NOVEL PHASE AT HIGH DENSITY AND THEIR ROLE IN THE STRUCTURE AND EVOLUTION OF NEUTRON STARS*

Sanjay Reddy

Center for Theoretical Physics, Massachusetts Institute of Technology
Cambridge, MA 02139, USA
and
Theoretical Division, Los Alamos National Laboratory
Los Alamos, New Mexico, NM 87545, USA

(Received October 21, 2002)

We present a pedagogic discussion on the role of novel phases of dense baryonic matter in "neutron" stars. Qualitative aspects of the physics that drives phase transitions and some of its astrophysical consequences are discussed. Observable aspects of neutron star structure and early evolution of the newly born neutron star are discussed in some detail.

PACS numbers: 12.38.Mh, 13.15.+g, 26.50.+x, 26.60.+c

1. Introduction

Despite decades of study, the question — *What is the ground state of dense baryonic matter?* — remains in the realm of theoretical speculation. Advances in our understanding of strongly interacting many-particle systems and QCD suggests numerous candidate states which have competitive free energy. Conventional many-body techniques, including those of lattice gauge theory and non-relativistic variational and Greens function methods, have yet to make definitive statements regarding the phase structure of matter at densities of relevance to neutron stars. In these lectures we discuss a few novel phases of matter and highlight some of their astrophysical consequences. They include *(i)* baryonic matter with hyperons, *(ii)* kaon condensation and *(iii)* normal and superconducting quark matter. The choice of topics presented is a synthesis of collaborative research the author has undertaken in the past four years. In this sense, the scope of the article is limited and no attempt is made to present a comprehensive review. For a detailed review of assorted topics relating to the interior of neutron stars see Ref. [1].

* Presented at the XLII Cracow School of Theoretical Physics, Zakopane, Poland May 31–June 9, 2002.

Terrestrial experiments, such as heavy-ion colliders, have been employed to probe new phases of matter that are likely to occur at high energy density. These experiments have proven to be useful in exploring the high temperature region of the phase diagram. They have had limited success in probing the high-density, low-temperature phases of QCD. Neutron stars are best suited to probe this region and thereby provide information that is complementary to terrestrial efforts. The first half of the lectures provide a lowbrow overview of plausible new phases inside neutron stars. In the latter part we discuss how these new phases will affect observable properties of neutron stars. In particular, we focus on the following topics to make contact with observables: *(i)* mass and radius, *(ii)* the birth and early evolution of newly born neutron stars in a supernova explosion, as evidenced by the neutrinos they emit.

2. Nucleonic matter

The thermodynamic properties of a many-particle system consisting of strongly interacting nucleons is difficult to calculate from first principles, even if the underlying Hamiltonian were known. Over the past several decades there have been numerous attempts to compute the bulk properties of nuclear and neutron-rich matter. These include microscopic many-body calculations using realistic nucleon–nucleon potentials and phenomenological relativistic and non-relativistic mean-field theories. The former approach starts with a potential that provides a good description of the measured nucleon–nucleon scattering data and uses variational or Greens function techniques to obtain the thermodynamic properties of the many-particle system. In mean field models the relation to nucleon–nucleon scattering is abandoned in favor of a simpler form of the interaction whose parameters are determined by fitting the model predictions to empirical properties of bulk nuclear matter at nuclear saturation density.

Walecka's field theoretical model in which the nucleons interact with ω, ρ and σ mesons provides a reasonable description of nuclei and nuclear matter [2]. It has been used extensively to study nuclear properties (for a review see Ref. [3]). The model we discuss supplements the original Walecka model with self-interactions between mesons and was introduced by Boguta and Bodmer [4]. The model Lagrangian is given by

$$\begin{aligned}\mathcal{L}_N &= \overline{\Psi}_N\Big(i\gamma^\mu\partial_\mu - m_N^* - g_{\omega N}\gamma^\mu V_\mu - g_{\rho N}\gamma^\mu\vec{\tau}_N\cdot\vec{R}_\mu\Big)\Psi_N \\ &\quad + \frac{1}{2}\partial_\mu\sigma\partial^\mu\sigma - \frac{1}{2}m_\sigma^2\sigma^2 - U(\sigma) - \frac{1}{4}V_{\mu\nu}V^{\mu\nu} \\ &\quad + \frac{1}{2}m_\omega^2 V_\mu V^\mu - \frac{1}{4}\vec{R}_{\mu\nu}\cdot\vec{R}^{\mu\nu} + \frac{1}{2}m_\rho^2\vec{R}_\mu\cdot\vec{R}^\mu\,, \end{aligned} \tag{2.1}$$

where Ψ_N is the nucleon field operator with $\vec{\tau}_N$ the nucleon isospin operator. Further, $m_N^* = m_N - g_{\sigma N}\sigma$ is the nucleon effective mass. This mass is reduced from the free nucleon mass m_N by the scalar field σ, taken to have $m_\sigma = 600$ MeV. The scalar self-interaction term is given by

$$U(\sigma) = \frac{b}{3} m_N (g_{\sigma N}\sigma)^3 + \frac{c}{4}(g_{\sigma N}\sigma)^4 , \tag{2.2}$$

where b and c are dimensionless coupling constants. The kinetic energy terms for the vector fields corresponding to the ω and ρ mesons involve $V_{\mu\nu} = \partial_\mu V_\nu - \partial_\nu V_\mu$, and $\vec{R}_{\mu\nu} = \partial_\mu \vec{R}_\nu - \partial_\nu \vec{R}_\mu$, respectively.

The five coupling constants, $g_{\sigma N}$, $g_{\omega N}$, $g_{\rho N}$, b, and c, are chosen as in Ref. [5] to reproduce five empirical properties of nuclear matter at saturation density: the saturation density itself is $n_0 = 0.16$ fm^{-3}; the binding energy per nucleon is 16 MeV; the nuclear compression modulus is 240 MeV; the nucleon effective mass at saturation density is $0.78 m_N$; and the symmetry energy[1] is 32.5 MeV.

The model is solved in the mean-field approximation, wherein only the time component of the meson fields have nonzero expectation values. The symbols σ_0, ω_0 and ρ_0 below denote expectation values that minimize the free energy. In the absence of neutrino trapping, charge-neutral stellar matter can be characterized by the baryon and electron chemical potentials since these are the only conserved charges. Weak interaction equilibrium ensures that $\mu_n - \mu_p = \mu_e$. The free energy density for such a system is given by [5]

$$\begin{aligned}
\Omega_{\rm nuclear}(\mu_B, \mu_e) &= -P(\mu_B, \mu_e) \\
&= \frac{1}{\pi^2}\left(\int_0^{k_{{\rm F}n}} dk\ k^2\ (\varepsilon_n(k) - \mu_n) + \int_0^{k_{{\rm F}p}} dk\ k^2\ (\varepsilon_p(k) - \mu_p) \right) \\
&\quad + \frac{1}{2}\left(m_\sigma^2 \sigma_0^2 - m_\omega^2 \omega_0^2 - m_\rho^2 \rho_0^2 \right) + U(\sigma_0) - \frac{\mu_e^4}{12\pi^2} ,
\end{aligned} \tag{2.3}$$

where $P(\mu_B, \mu_e)$ is the pressure, $\mu_B = \mu_n$ is the baryon chemical potential and

$$\varepsilon_n(k) = \sqrt{k^2 + {m_N^*}^2} + g_{\omega N}\omega_0 - \tfrac{1}{2} g_{\rho N}\rho_0 , \tag{2.4}$$

$$\varepsilon_p(k) = \sqrt{k^2 + {m_N^*}^2} + g_{\omega N}\omega_0 + \tfrac{1}{2} g_{\rho N}\rho_0 , \tag{2.5}$$

are the neutron and proton single particle energies in the mean field approximation. The corresponding Fermi momenta $k_{{\rm F}n}$ and $k_{{\rm F}p}$, which minimize

[1] The energy that depends on the difference in neutron and proton densities.

the free energy at fixed baryon and electron chemical potentials, are given by solving

$$\begin{aligned} \varepsilon_n(k_{\mathrm{F}n}) &= \mu_n \,, \\ \varepsilon_p(k_{\mathrm{F}p}) &= \mu_p \,. \end{aligned} \tag{2.6}$$

Further, the mean field expectation values for the meson fields that minimize Eq. (2.3) are given by

$$\begin{aligned} m_\sigma^2 \sigma_0 &= g_{\sigma N} \left(n_s(k_{\mathrm{F}n}) + n_s(k_{\mathrm{F}p}) \right) - \frac{dU}{d\sigma} \,, \\ m_\omega^2 \omega_0 &= g_{\omega N} \left(n_B(k_{\mathrm{F}n}) + n_B(k_{\mathrm{F}p}) \right) \,, \\ m_\rho^2 \rho_0 &= \tfrac{1}{2} g_\rho \left(n_B(k_{\mathrm{F}p}) - n_B(k_{\mathrm{F}n}) \right) \,, \end{aligned} \tag{2.7}$$

where baryon number and scalar densities, n_B and n_s, respectively, are given by

$$\begin{aligned} n_B(k_{\mathrm{F}}) &= \langle \Psi_N^\dagger \Psi_N \rangle = \sum_{i=n,p} \frac{1}{\pi^2} \int_0^{k_{\mathrm{F}i}} dk\, k^2 \,, \\ n_s(k_{\mathrm{F}}) &= \langle \bar{\Psi}_N \Psi_N \rangle = \sum_{i=n,p} \frac{1}{\pi^2} \int_0^{k_{\mathrm{F}i}} dk\, k^2 \frac{m_N^*}{\sqrt{k^2 + {m_N^*}^2}} \,. \end{aligned} \tag{2.8}$$

Note that in Eq. (2.3) the electron contribution to the free energy has also been included. In bulk matter the condition $\partial \Omega_{\mathrm{nuclear}} / \partial \mu_e = 0$, which enforces electric-charge neutrality, uniquely determines μ_e. The magnitude and the density dependence of the electron chemical potential is sensitive to the value of the nuclear symmetry energy, parametrized in this model as the strength of the isovector interaction.

The model described above provides us with a simple tool to understand the various forces at play in the description of charge-neutral nucleonic matter in weak equilibrium. To study possible phase transitions we will employ this model to represent the nuclear phase. Differences between the simple model employed here and detailed many-body calculations can, however, be important at high densities. This will influence both the location and the nature of the phase transitions between the nuclear and more exotic phases to be considered below. Nonetheless, the *qualitative* aspects of the phase transitions are generic and are observed even in the most sophisticated many-body descriptions of the nuclear phase.

Fig. 1 shows the thermodynamic properties of charge-neutral stellar matter calculated using the mean-field model. The left panel shows the baryon

chemical potential, electron chemical potential and the energy per particle as a function of the baryon density, normalized to the nuclear saturation density $n_0 = 0.16$ fm^{-3}. The right panel shows energy density as a function of pressure and is usually referred to as the Equation of State (EoS). It is this relation that is required to solve for the structure of the neutron star and therefore determines neutron star the mass and radius.

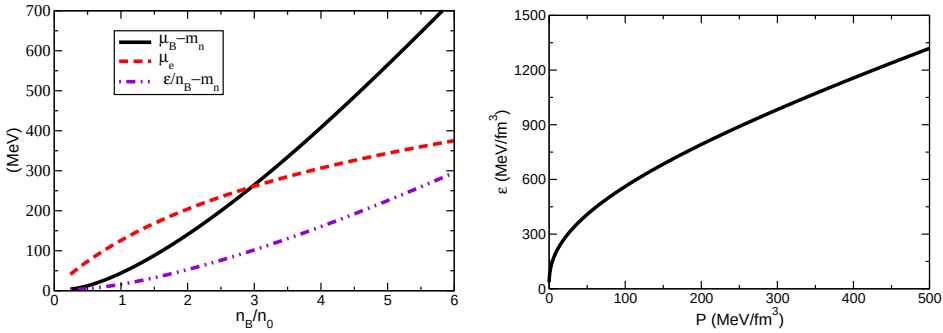

Fig. 1. The nuclear equation of state. The left panel shows the density dependence of the baryon chemical potential, the electron chemical potential and the energy per baryon. The right panel shows the relation between energy density and pressure.

3. Novel phases

With increasing density the chemical potentials for baryon number and negative electric-charge increase rapidly due to the repulsive nature of strong interactions at short distances. This furnishes energy for the production of strange baryons and the condensation of mesons. At even higher densities our knowledge of QCD and its asymptotic behavior leads us to expect that the quarks inside nucleons will delocalize and form a uniform Fermi sea of quarks. These expectations are borne out by model calculations of these phases. In what follows we consider a few of these scenarios in detail.

3.1. Hyperons

Fig. 2 shows the variation of chemical potential associated with neutral and charged baryons. The thick solid curves are predictions of the mean field model described in the previous section and the thin lines correspond to the non-interacting Fermi gas model. The upper curve in each of the above-mentioned cases corresponds to baryons with negative charge, the middle curve to neutral baryons and the lowest curve corresponds to baryons with positive charge. The upper and lower horizontal dashed lines indicate the vacuum masses of the $\Sigma^{\pm}$ and the Λ hyperons, respectively. The location

where the chemical potentials cross the vacuum masses are also indicated for the interacting case. This analysis neglects the strong interactions the between hyperons and nucleons. If they were on-average attractive, the corresponding second-order phase transitions would occur at lower density. On the other hand, if they were repulsive, the transitions would be pushed to higher densities. Note also that strong interactions between nucleons also plays an important role in determining the transition density. For the case of non-interacting nucleons the transitions occur at densities that are significantly larger. The baryon chemical potential in all models which incorporate strong interactions will be larger than the naive prediction of the free Fermi gas model at high densities. This generic feature arises because strong interactions at short distances are repulsive.

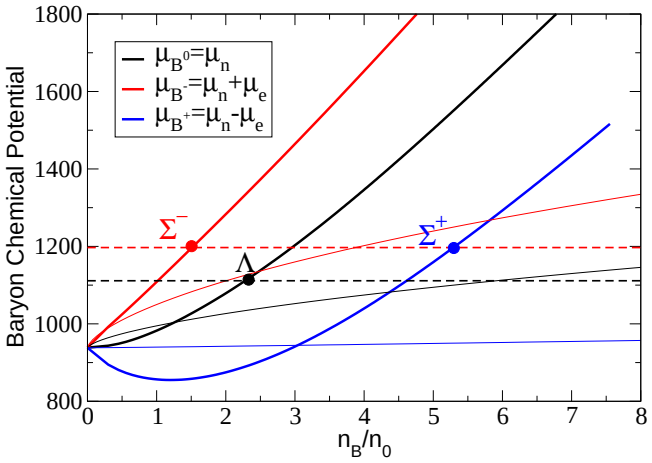

Fig. 2. Baryon chemical potentials in dense stellar matter computed with (mean-field model, thick curves) and without (free Fermi gas model, thin curves) strong interactions are shown. In each case, the upper most curve is for negatively-charged baryons, the middle curve is for neutral baryon and the lower curve is for positively-charged baryons.

These are second-order transitions because we are only considering the energy cost for introducing infinitesimal hyperon populations. If the hyperon–hyperon interactions are strongly attractive, these phase transitions can become first-order. In this case it is energetically favorable to have many hyperons appear together rather than for their population to grow infinitesimally.

Hyperon–nucleon interactions are poorly constrained due to the lack of experimental data. The exception is the Λ binding energy in hypernuclei [6]. This information was first employed in mean field models by Glendenning [7].

Hyperons are introduced into the mean-field model discussed in section 2 by minimal coupling to the σ, ω and ρ mesons, and there arise three corresponding couplings constants that must be constrained. The binding energy of the Λ provides one constraint which relates the $g_{H\sigma}$ and $g_{H\omega}$, since the Λ carries no isospin, and additionally the ρ meson mean field vanishes in isospin symmetric matter. In the simplest mean-field model, the hyperon couplings to the vector meson couplings are chosen to be similar to 2/3 of that of the nucleons. This choice is partially motivated by simple quark number and isospin counting rules. The Λ binding energy is then used to determine the strength of the coupling to the σ meson. The model further assumes that the all hyperons couple to the mesons with the same strength. This is likely to be a serious drawback of this simple model. There are several direct and indirect indications coming primarily from studies of Σ^- atoms[2] that indicate the Σ^- experiences a repulsive interaction in nuclear matter [8].

To summarize, strong interactions between nucleons result in a rapid increase of the baryon chemical potential at high density. The baryon chemical potential is typically larger than the lightest hyperon masses at a baryon density between 1–3 times nuclear density. Experimental inputs indicate that strong interactions between Λ particles and nucleons are attractive and this acts to lower the density for their appearance. The situation with the Σ^- is less clear since experiment suggests that they experience repulsive interactions in nuclei, even though the presence of a negative-charge chemical potential in neutron stars favors their appearance.

Hyperons contribute more to the energy density of matter than to the pressure as compared to nucleons. This is easily understood by noting that they have larger masses and have smaller Fermi momenta. The change in energy density per unit change in pressure is large relative to the nuclear case, and this behavior is usually referred to as softening of the EoS. As we will discuss in subsequent sections this will act to reduce both the maximum mass and the radius of neutron stars. Hyperons can also influence transport properties and the thermal evolution of the star since they furnish new degrees of freedom that are less degenerate than the nucleons, which can more readily participate in dissipative processes.

3.2. Kaon condensation

A large number of electrons are required to ensure charge neutrality in dense nuclear matter. The typical electron chemical potential μ_e is about 100 MeV at nuclear density. With increasing density, μ_e increases to keep pace with the increasing proton number density. The magnitude of this

[2] This is an electromagnetic bound state of Σ^- and a nucleus.

increase depends sensitively on the density dependence of the isovector interaction contribution to the nuclear symmetry energy. In Fig. 3 the density dependence of the electron chemical potential in the mean-field model is shown as the thick black curve. For reference, the electron chemical potential for the case of non-interacting nucleons is also shown (thin black line). Negatively charged bosons whose rest energy in the medium is less than the electron chemical potential will condense via a second-order phase transition. The extent of condensation will be regulated by repulsive interactions between bosons in the s-wave channel at low momenta.

In the hadronic phase the likely candidates for condensation are the π^- and the K^-. In vacuum, pions are significantly lighter than kaons, but this situation may be reversed in the dense medium due to strong interactions between mesons and nucleons. The physical basis for this expectation is that the effective theory of meson–nucleon interactions, such as chiral perturbation theory, must incorporate the repulsive s-wave interactions arising due to the Pauli principle between the constituent quarks inside nucleons and mesons. Mesons containing u or d quarks will experience repulsion, while on the other hand, mesons containing $\bar{u}$ or $\bar{d}$ quarks and s (*i.e.*, kaons) quarks will experience attraction in the nuclear medium[3]. Experiments with kaonic atoms lend strong support to the aforementioned theoretical expectation of attraction [9].

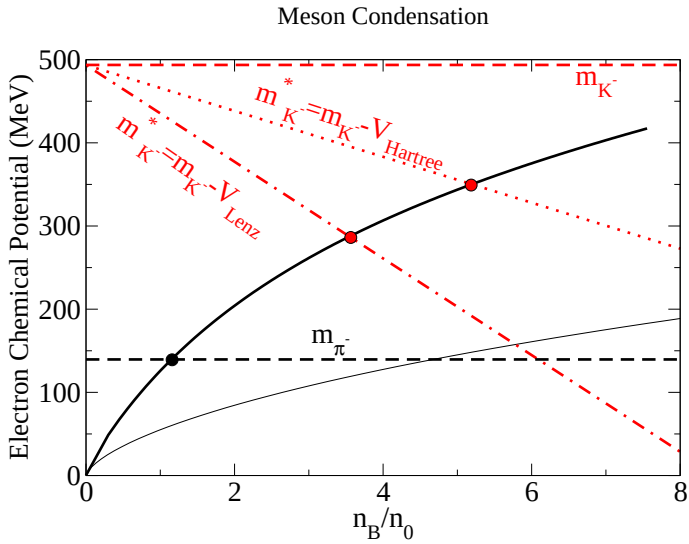

Fig. 3. Electron chemical potential, the pion and kaon vacuum and in-medium effective masses in dense stellar matter.

[3] This simple explanation is due to David Kaplan.

In Fig. 3 the vacuum pion and kaon masses are shown as the dashed lines. If the masses do not change in the medium, the figure indicates that π^- condensation occurs in the vicinity of nuclear density and that K^- condensation does not occur for the densities considered. When interactions with medium are included, however, a uniformly charged pion condensate is disfavored due to a weak repulsive s-wave interaction. Instead, a spatially varying condensate can be favored due to attractive p-wave interactions (for a review see Ref. [10]). The kaon–nucleon interaction, on the other hand, is *strongly* attractive. In what follows we only discuss kaon condensation for this simple reason.

The idea that kaons could condense in dense nuclear matter was due to Kaplan and Nelson [11]. Using a simplified $\mathrm{SU_R}(3) \otimes \mathrm{SU_L}(3)$ chiral Lagrangian they showed that the K^- could condense at a density about three times nuclear density. Subsequently several authors have studied in detail the nature and the role of kaon condensation in neutron star matter (for a recent review see Ref. [12]).

Here, we will employ a simple schematic potential model for kaon–nucleon interactions considered in Ref. [13] to illustrate the salient features. The scattering length a_{K^-n} characterizes the low energy kaon–nucleon interaction, and experiment indicates that $a_{K^-n} \approx -0.4$ fm. Following the authors of Ref. [13] we will assume that the interaction potential can be modeled as a square well. The parameters of the potential, *i.e.*, the depth $V_0 = -122$ MeV and range $R = 0.7$ fm, are determined by fitting to low energy nucleon–kaon data (for further details see Ref. [13]). Given this potential the change in the effective mass of K^- in a low-density medium of neutrons can be computed using the Lenz approximation. In this approximation the attractive potential energy experienced by a kaon at rest can be directly related to the scattering length and is given by

$$V_{\mathrm{Lenz}} = -\frac{2\pi}{m_{Kn}}\, a_{K^-n}\, n_n\,, \tag{3.1}$$

where m_{Kn} is the reduced mass of the neutron–kaon system and n_n is the neutron density. The effective mass of the kaon computed using Eq. (3.1) is shown in the Fig. 3. In this case, the kaon effective mass equals the electron chemical potential when $n_n \sim 3-4$ times nuclear density. This corresponds to the critical density for kaon condensation.

At higher densities, the Hartree or mean field approximation is expected to be valid. In this case the attractive potential energy of the kaon cannot be related directly to on-shell low energy kaon–nucleon scattering data. The Hartree potential is given by

$$V_{\mathrm{Hartree}} = \frac{4\pi}{3}\, V_0\, R^3\, n_n\,, \tag{3.2}$$

where V_0 and R are the depth and range of the K^--n potential. Fig. 3 indicates that kaons would condense in the Hartree approximation when $n_n \sim 5$–6 times nuclear density.

3.3. Normal quark matter

The occurrence of the novel hadronic phases mentioned above depends sensitively on the nature of hadronic interactions and their many-body descriptions. In contrast, the asymptotic behavior of QCD, which requires that interactions between quarks become weak with increasing momenta, provides strong support to the notion that at sufficiently high densities nucleonic degrees of freedom must dissolve to form a nearly free (perturbative) gas of quarks. The precise location of this phase transition will depend on model descriptions of both the nuclear and quark phases. This is because all model studies indicate that the phase transition occurs at rather low densities where perturbative methods do not apply.

The bag model provides a simple description of quark matter and confinement. The model was designed to provide a description of the hadron mass spectrum. The basic tenants of the model are a non-trivial vacuum and nearly free quark propagation in spaces (bags) wherein the perturbative vacuum has been restored. This restoration costs energy since it requires the expulsion of the vacuum condensates. The restoration energy per unit volume is called the bag constant and is denoted as B. The model also provides a very simple and intuitive description of bulk quark matter. The pressure in the bulk quark phase containing up (u), down (d) and strange (s) quarks is due to the kinetic energy density of quarks and a negative bag pressure. At zero temperature this is given by

$$P_{\rm Bag}(\mu_u,\mu_d,\mu_s) = -\Sigma_{i=u,d,s} \int_0^{k_{{\rm F}i}} \frac{\gamma\, d^3k}{(2\pi)^3}(\sqrt{k^2+m_i^2}-\mu_i) \; - B\,, \qquad (3.3)$$

where $\gamma = 2_{\rm spins} \times 3_{\rm color}$ is the degeneracy factor and $k_{{\rm F}i}$ is the Fermi momentum of each quark flavor. The chemical potential for each flavor $\mu_i = \sqrt{k_{{\rm F}i}^2 + m_i^2}$, where m_i is the corresponding quark mass. In the limit of massless quarks and a common chemical potential for all the quarks, the pressure in the bag model has the following simple form

$$P_{\rm Bag}(\mu) = \frac{3}{4\pi^2}\mu^4 - B\,, \qquad (3.4)$$

where $\mu = \mu_B/3$ is the quark chemical potential. The pressure of bulk quark matter computed using the Eq. (3.3) for $B^{1/4} = 150$ MeV and $B^{1/4} = 200$

MeV are shown in Fig. 4. The phase with the largest pressure is favored and the figure shows that the nuclear-quark transition density is very sensitive to the bag constant. For the case when $B^{1/4} = 150$ MeV (the upper most curve), three flavor quark matter is the true ground state of matter and nuclear matter is a metastable state [16]. For larger values of B the transition occurs at higher densities.

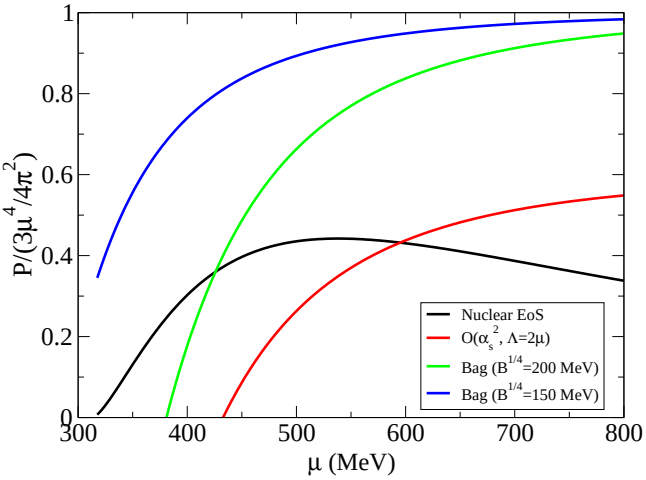

Fig. 4. Pressure *vs* baryon chemical potential for several quark matter EoS models. The pressure in the nuclear mean field model is also shown for reference.

Leading order effects of perturbative interactions between quarks can also be incorporated in the bag model at high density. This has the effect of renormalizing the kinetic term. The pressure in this case is given by

$$P_{\mathrm{bag},\alpha_s}(\mu) = \frac{3}{4\pi^2}\left(1 + \frac{2\,\alpha_s}{\pi}\right)\mu^4 - B\,, \tag{3.5}$$

where $\alpha_s = g^2/4\pi$ and g is the QCD coupling. At densities of relevance to neutron stars, perturbative expansion in α_s is not valid. Nonetheless, it is still interesting to note that the order α_s^2 calculation of the free energy predicts a behavior that is similar to that of bag model [14, 15]. Recently, Fraga, Pisarski and Schaffner–Bielich recomputed the equation of state of massless quark matter to $O(\alpha_s^2)$. They find that the perturbative result is well reproduced by the following bag-model-inspired form for the pressure over a wide range of densities relevant to neutron stars [15],

$$P_{\mathrm{perturb}}(O(\alpha_s^2),\mu) = \frac{3}{4\pi}a_{\mathrm{eff}}\mu^4 - B_{\mathrm{eff}}\,, \tag{3.6}$$

where $a_{\rm eff} = 0.628$ and $B_{\rm eff}^{1/4} = 199$ MeV for the specific choice for the renormalization subtraction point, $\Lambda = 2\mu$. The pressure obtained using Eq. (3.6) is also shown in Fig. 4. In the order $\alpha_{\rm s}^2$ calculation, the transition occurs at even higher density compared to the case when $B^{1/4} = 200$ MeV.

To summarize, much like in the case of hyperons and kaons, quark matter softens the equation of state. The softening is both due to a larger number of degrees of freedom in the quark phase and the bag constant which makes a negative contribution to the pressure and a positive contribution to the energy density.

3.4. Superconducting quark matter

Since the early work of Bardeen, Cooper and Schrieffer it has been well known that degenerate Fermi systems are unstable in the presence of arbitrarily weak attractive interactions at the Fermi surface [17]. The instability is resolved by the formation of a Bose condensate of Cooper pairs. As is well known, for the case of charged fermions, like electrons, this leads to superconductivity. In analogy, the presence of attractive interactions between quarks will lead to pairing and color superconductivity. This was realized several decades ago in early work by Barrios and Frautschi [18]. Recent realization that the typical superconducting gaps in quark matter are larger than those predicted in these early works has generated renewed interest. Model estimates of the gap at densities of relevance to neutron stars suggest that $\Delta \sim 100$ MeV when $\mu = 400$ MeV [19]. Excellent accounts of these recent findings can be in Ref. [20]. In what follows, we provide a brief introduction to the subject and emphasize aspects that impact neutron star phenomenology.

It is simple to verify that the One-Gluon-Exchange (OGE) potential between quarks is attractive in the antisymmetric (color-triplet) channel, such as $(r_1 b_2 - b_1 r_2)/\sqrt{2}$. The potential is given by $V_{qq}^A = -2\alpha_{\rm s}/3r$. Similarly, the OGE quark–quark potential in the symmetric (color-sextet) channel is repulsive, and the potential is $V_{qq}^S = \alpha_{\rm s}/3r$. The attraction in the triplet channel can result in s-wave pairing between quarks in spin zero and spin one channels. Explicit calculations show that the pairing energy, Δ, is especially large for the spin-zero case. This type of pairing can only occur between unlike flavors of quarks to ensure that the diquark pair (which is a boson) has a wavefunction that is symmetric.

For three massless flavors the condensation pattern that minimizes the free energy is called the color-flavor-locked scheme [21]. Pairing occurs between states that are on opposite sides of the Fermi surface. For massless particles the spin-zero state involves either only left and only right-handed quarks. The non-zero condensates in this phase are given by

$$\langle \psi_{a,{\rm L}}^{i\alpha} \psi_{b,{\rm L}}^{j\beta} \varepsilon_{ij} \rangle = -\langle \psi_{a,{\rm R}}^{i\alpha} \psi_{b,{\rm R}}^{j\beta} \varepsilon_{ij} \rangle \;=\; \Delta\; \varepsilon^{\alpha\beta A}\; \varepsilon_{abA} = \Delta\; (\delta_a^\alpha \delta_b^\beta - \delta_b^\alpha \delta_a^\beta)\,, \quad (3.7)$$

where α, β are color indices, a, b are flavor indices, and i, j are spinor. The Levi–Civita symbols in spinor space, in flavor space and in color space ensures that the pair has spin-zero, and is anti-symmetric in flavor and color space respectively. The last equality of this equation explicitly shows that the condensation locks color and flavor indices.

The choice of the colors and flavors that are locked, is of course, arbitrary. For one particular choice the pairing scheme is illustrated in Fig. 5 [4]. In the

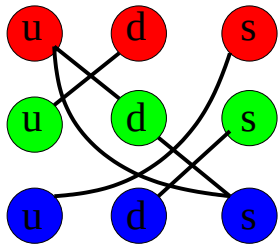

Fig. 5. Pairing scheme in color-flavor-locked quark matter. The different rows (columns) correspond to different colors (flavors).

Color–Flavor-Locked phase (CFL henceforth) all nine quarks participate in pairing. Consequently, the energy required to create a quark excitation involves the breaking of a Cooper pair and the fermion excitation spectrum is characterized by an energy gap $\sim 2\Delta$. Further, gluons acquire a mass via the Higgs mechanism by coupling to the colored condensates. The lowest energy collective excitations in this phase correspond to Goldstone bosons. The number and spectrum of these Goldstone modes can be understood by noting that the condensate breaks baryon number and chiral symmetries. Baryon number is broken because the CFL state is not an eigenstate of the baryon number operator. This is completely analogous to superconducting state of electrons, where the BCS ground state is not an eigenstate of the electron number.

The CFL state breaks chiral symmetry by a novel mechanism [21]. Left and right-handed condensates are coupled because the color exchange is a vector interaction. Flavor rotations on the L condensate must be compensated by a rotation of the R condensate [21], and therefore chiral symmetry is spontaneously broken. The octet of flavor Goldstone bosons that result will acquire a mass because quark masses explicitly break chiral symmetry. The quantum numbers of these pseudo-Goldstone modes maps onto the meson octet in vacuum. For this reason they are often commonly referred to as the "pions" and "kaons" (or collectively as "mesons") of the high-density

[4] This picture illustration was suggested by George Bertsch.

phase. Their masses have been computed in earlier work by matching the high density chiral effective theory to perturbative QCD. Unlike the vacuum case, the square of "meson" masses here is proportional to the product of quark masses [22]. This results in an inverted hierarchy, where the pions are heavier than the kaons. Explicitly, at high density the masses are given by

$$\begin{aligned} m^2_{\pi^\pm} &= a(m_u + m_d)m_s\,, \\ m^2_{K^\pm} &= a(m_u + m_s)m_d\,, \\ m^2_{K^0} &= a(m_d + m_s)m_u\,, \end{aligned} \tag{3.8}$$

where $a = 3\Delta^2/\pi^2\mu^2$. In contrast, the baryon number Goldstone boson remains massless. This singlet mode is responsible for the superfluid nature of this phase [21]. As will be discussed in detail in subsequent sections, this massless mode also plays a crucial role in determining the neutrino opacity of the CFL phase.

Pairing at the Fermi surface also contributes to the pressure, which on dimensional grounds, we can expect to be $\sim \Delta^2\mu^2$. For three massless flavors, we can supplement the bag model pressure with the contribution due to superconductivity. In the CFL phase it is given [23]

$$P_{\rm CFL} = \frac{3}{4\pi^2}\,\mu^4 + \frac{3}{\pi^2}\,\Delta^2\mu^2 - B\,, \tag{3.9}$$

which is to be compared with Eq. (3.4).

It is a reasonable approximation to neglect the u and d quark masses at densities of relevance to neutron stars where $\mu \sim 400$ MeV. The strange quark mass $m_s \sim 200$ MeV, on the other hand, cannot be neglected. The difference in Fermi momenta between light quarks and the strange quark is $\sim m_s^2/2\mu$. Thus, when $\Delta \lesssim m_s^2/2\mu$, pairing involving strange quarks will be suppressed. In the limit of infinite strange quark mass, *i.e.*, in their absence, only light quarks pair. This phase is called 2SC (two-flavor superconductor) and it is also characterized by pairs that are antisymmetric in flavor [19]. Antisymmetry in color space excludes one of the three colors from participating in the condensation. Thus $\mathrm{SU}(3)_{\rm color}$ is broken down to $\mathrm{SU}(2)_{\rm color}$. Quarks of a particular color and three gluons remain massless. Further, unlike the CFL phase, no global symmetries are broken. The absence of the massless Goldstone bosons implies the absence of the superfluidity. In this sense, the 2SC phase appears quite unremarkable.

Early attempts to bridge the "gap" between the 2SC phase and the CFL phase can be found in Ref. [24,25]. They found that the CFL pairing scheme is preserved when $m_s \lesssim \sqrt{2\mu\Delta}$. For larger m_s a first-order transition to the 2SC phase occurs. The response of the CFL phase to a finite strange quark mass in these earlier works ignored the role of the flavor Goldstone modes.

Bedaque and Schafer showed that the strange quark mass appeared in the effective theory for Goldstone bosons in the form of a chemical potential for anti-strangeness [26]. Since $m_u < m_d$, K^0 is the lightest Goldstone mode with anti-strangeness in the high-density effective theory (see Eq. (3.8)). Consequently, when the chemical potential, $\mu_{\bar{s}} \sim m_s^2/2\mu$, exceeds the mass of the K^0 boson they will condense in the ground state. Using the asymptotic formula for the meson masses given in Eq. (3.8), Bedaque and Schafer showed that K^0 condensation occurs when $m_s \gtrsim (m_u \Delta^2)^{1/3}$. The phase with a K^0 condensate is distinct from the CFL phase as it breaks additional symmetries. However, since the pairing scheme itself remains unaltered we label this phase CFL$\,K^0$ [27]. In the presence of quark masses and chemical potentials, the CFL phase is symmetric under $\mathrm{U}(1)_Y \otimes \mathrm{U}(1)_{\tilde{Q}}$ rotations, where Y is hypercharge or strangeness and $\tilde{Q}$ is the modified electric-charge in the CFL phase. In the CFL$\,K^0$ phase hypercharge or strangeness symmetry is spontaneously broken, resulting in the appearance of a massless Goldstone boson.

Much like the strange-quark mass, the presence of an electric-charge chemical potential will act as source to condense charged mesons in the CFL phase if its strength exceeds the mass of the lightest charged boson. In the CFL phase, K^+ and π^- are the lowest energy charged-particle excitations. (The K^- excitations cost more energy due to the presence of the anti-strange chemical potential induced by the strange quark mass.) The phase diagram in the presence of an electric charge chemical potential and the strange quark mass exhibits a rich structure. For a detailed discussion of these novel meson condensed phases and their roles in the birth and evolution of neutron stars see Ref. [27].

An interesting feature of BCS-like pairing in simple systems with only two degrees of freedom is the locking of the Fermi surfaces in momentum space. Consider pairing between massless u and d quarks in the presence of an electric-charge chemical potential. The charge chemical potential in the absence of the pairing interaction will act to change the relative number of u and d quarks. In the presence of pairing the state resists this change. With increasing electric-charge chemical potential the system exhibits no response up to a critical value. When the difference in chemical potentials between the particles participating in the pairing exceeds 2Δ, the system responds via a first-order transition to the unpaired normal state. This rigidity was initially thought to ensure equal numbers of u, d and s quarks in the CFL phase, despite the strange quark mass [28]. A detailed analysis, however, shows that rigidity in the color-flavor-locked phase takes on a different form [29]. It enforces equality between the color and flavor quark number of those colors and flavors that are locked by pairing. For the pairing scheme shown

in Fig. 5 rigidity manifests in the form of the following equations [29]

$$n_r = n_u\,, \qquad n_g = n_d\,, \qquad n_b = n_s\,. \tag{3.10}$$

The above relations, combined with the additional condition of local color neutrality, ensure equal numbers of u, d and s quarks [29]. Therefore, despite the strange quark mass, the CFL and the CFLK^0 phases are electrically neutral. No electrons are present and there are no massless charged-particle excitations. Thus, with regard to electromagnetism, the CFL phase is a transparent insulator [30].

4. Nature of the phase transition

The novel phases discussed above could occur either via a first or second-order phase transition. In the latter case, the order parameter for the new phase is infinitesimal at the critical density and smoothly grows with increasing density. In these situations the electric-charge chemical potential is also able to adjust smoothly to maintain charge neutrality in the bulk phase. On the other hand, in the case of first-order phase transitions the order parameter characterizing the new phase has a finite value at the onset of the transition. The electric-charge chemical potential required to ensure neutrality changes discontinuously across the transition. In these situations the presence of two conserved charges, namely baryon number and electric charge, allows for the possibility of phase co-existence, *i.e.*, satisfies the Gibbs criterion of equal chemical potentials and pressure.

This phase with two co-existing phases is often referred to as the mixed phase. Charge neutrality is enforced globally. The two co-existing phases, in our case the nuclear phase and the denser exotic phase, have opposite electric-charges, and carry positive and negative charge respectively. The volume fraction occupied by the exotic phase adjusts to ensure overall electric-charge neutrality. Denoting the volume fraction of the denser phase as χ, global charge neutrality requires

$$\chi\; Q_{\rm exotic} + (1-\chi)\; Q_{\rm nuclear} = 0\,. \tag{4.1}$$

This was first noted by Glendenning [31] in the context of high density phase transitions. The phase co-existence occurs over a finite interval in pressure due to the presence of the extra degree of freedom, namely electric-charge. However, as we discuss next, the extent and existence of such a mixed phase depends on surface tension between the two phases.

To illustrate the physics of first-order phase transitions and the role of surface and Coulomb energies in the mixed phase we consider an explicit example. The phase transition from nuclear matter to CFL quark matter is

first-order. The nuclear phase has no strangeness and the bulk quark phase has no electrons. The possibility of phase co-existence between these phases was investigated in Ref. [23]. We highlight some of the main findings here. A schematic phase diagram is shown in Fig. 6. The nuclear and CFL phases are favored in the lower-left and upper-right shaded regions, respectively. With increasing baryon chemical potential, the electron chemical potential in the charge-neutral nuclear phase grows, as shown by the solid curve that ends at the point labeled A. Nuclear matter is positively charge in the region below this curve and negatively charged in the region above. Similarly, the CFL phase is electrically neutral when $\mu_e = 0$, and is negatively (positively) charged when $\mu_e > 0$ ($\mu_e < 0$). When μ_e exceeds the mass of the lightest negatively charged Goldstone mode these modes condense (via a second-order phase transition) to provide an additional contribution to the electric-charge density [23]. A positively charged nuclear phase and a negatively charged CFL phase can coexist along the line formed by the intersection of the two shaded regions (from A–D). Along this line, which defines the mixed phase, both phases have equal pressure and chemical potentials, *i.e.*, they satisfy the Gibbs criteria.

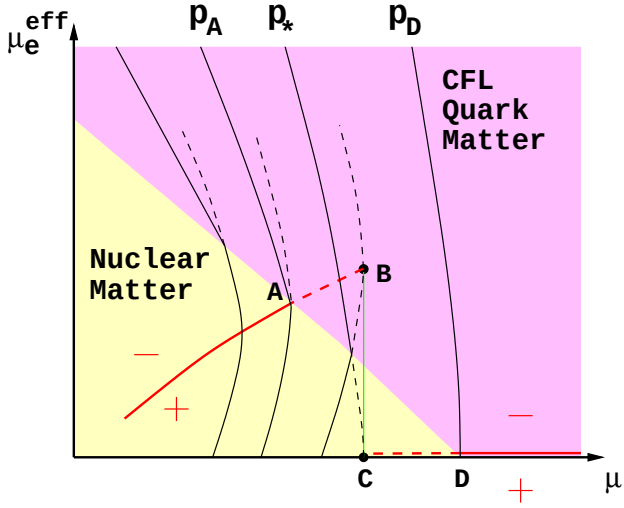

Fig. 6. A schematic phase diagram showing the nuclear and CFL phases in the plane of quark chemical potential μ and effective electron chemical potential μ_e. Isobars are shown as thin solid lines, and neutrality lines for nuclear and CFL matter are thick lines. Each phase is negatively charged above its neutrality line, and positively charged below it. Continuation onto the unfavored sheet is shown by broken lines [23].

In Fig. 7, a more detailed version of Fig. 6, the pressure of the bulk nuclear, bulk CFL and mixed phases are shown as a function of μ, the quark chemical potential. At intermediate values of μ, the mixed phase has larger pressure and is therefore favored over both the nuclear and CFL bulk phases. The electron chemical potential, μ_e, required to ensure charge neutrality in the bulk nuclear phase, grows with μ as shown. In the mixed phase neutrality requires a positively-charged nuclear phase and a negatively-charged CFL phase. This is easily accomplished by lowering μ_e from that required to maintain charge neutrality in the nuclear phase (see Fig. 6). The rate at which μ_e decreases in the mixed phase is shown in the figure and is obtained by requiring equal pressures in the both phases at a given μ.

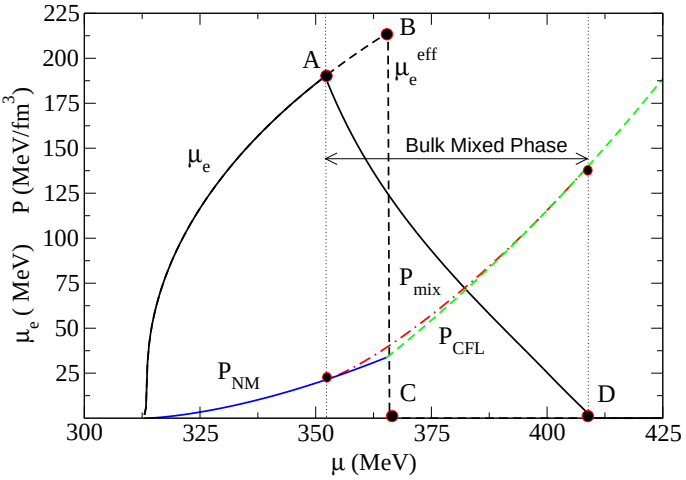

Fig. 7. Behavior of the electron chemical potential and the pressure of homogeneous neutral nuclear matter, CFL matter and of the mixed phase, all as a function of the quark chemical potential μ. Only bulk free energy is included; surface and Coulomb energy is neglected. The mixed phase occurs between A and D. The vertical line connecting B and C denotes the μ at which the pressures of neutral CFL and nuclear matter are equal. This is where a sharp interface may occur. The pressure of the mixed phase exceeds that of neutral CFL or neutral nuclear matter between A and D [23].

As noted earlier, in the mixed phase the Coulomb and surface energy costs must be met. The results shown in Fig. 7 ignore these corrections. In a simple description of the mixed phase one considers a sharp boundary between the coexisting phases. A unit cell of the mixed phase is defined as the minimum-size region that is electrically neutral. Three different simple geometries are considered: spheres, rods and slabs [32]. In each of these

cases, the surface and Coulomb energy cost per unit volume are given by

$$E^{\rm S} = \frac{d\ x\ \sigma_{\rm QCD}}{r_0}\,, \tag{4.2}$$

$$E^{\rm C} = 2\pi\ \alpha_{\rm em} f_d(x)\ (\Delta Q)^2\ r_0^2\,, \tag{4.3}$$

where d is the dimensionality of the structure ($d = 1, 2$, and 3 for slab, rod and droplet configurations, respectively), σ is the surface tension, and $\Delta Q = Q_{\rm nuclear} - Q_{\rm CFL+kaons}$ is the charge-density contrast between the two phases. The other factors appearing in Eqs. (4.2), (4.3) are: x, the fraction of the denser phase; r_0, the radius of the rarer phase (radius of drops or rods and half-thickness of slabs); and $f_d(x)$, the geometrical factor that arises in the calculation of the Coulomb energy which can be written as [32]

$$f_d(x) = \frac{1}{d+2}\ \left(\frac{2 - d\ x^{1-2/d}}{d-2} + x\right)\,. \tag{4.4}$$

The first step in the calculation is to evaluate r_0 by minimizing the sum of $E^{\rm C}$ and $E^{\rm S}$. The result is

$$r_0 = \left[\frac{d\ x\ \sigma_{\rm QCD}}{4\pi\ \alpha_{\rm em} f_d(x)\ (\Delta Q)^2}\right]^{1/3}\,. \tag{4.5}$$

We then use this value of r_0 in Eqs. (4.2), (4.3) to evaluate the surface and Coulomb energy cost per unit volume

$$E^{\rm S} + E^{\rm C} = \frac{3}{2}\left(4\pi\ \alpha_{em}\ d^2\ f_d(x)\ x^2\right)^{1/3}\ (\Delta Q)^{2/3}\ \sigma_{\rm QCD}^{2/3}\,, \tag{4.6}$$

where x equals χ when $\chi \leqslant 0.5$ and $(1-\chi)$ when $0.5 \leqslant \chi \leqslant 1$. The dependence $\chi(\mu)$ is computed using Eq. (4.1).

We must now compare this cost to the bulk free energy benefit of the mixed phase. The lowest curve in Fig. 8 shows $\Delta\Omega$, the difference between the free energy density of the mixed phase (calculated without the surface and Coulomb energy cost) and the homogeneous electrically neutral nuclear and CFL phases separated by a single sharp interface, whichever of the two is lower. The mixed phase has lower bulk free energy, so $\Delta\Omega$, plotted in Fig. 8, is negative. The remaining curves in Fig. 8 show the sum of the bulk free energy difference $\Delta\Omega$ and $(E^{\rm S} + E^{\rm C})$, the surface and Coulomb energy cost of the mixed phase calculated using Eq. (4.6) for droplets, rods and slabs. We employ three different values of $\sigma_{\rm QCD}$ since the QCD surface tension is, as yet, not very well known. Careful inspection of the figure reveals that for any value of $\sigma_{\rm QCD}$, the mixed phase is described as a function

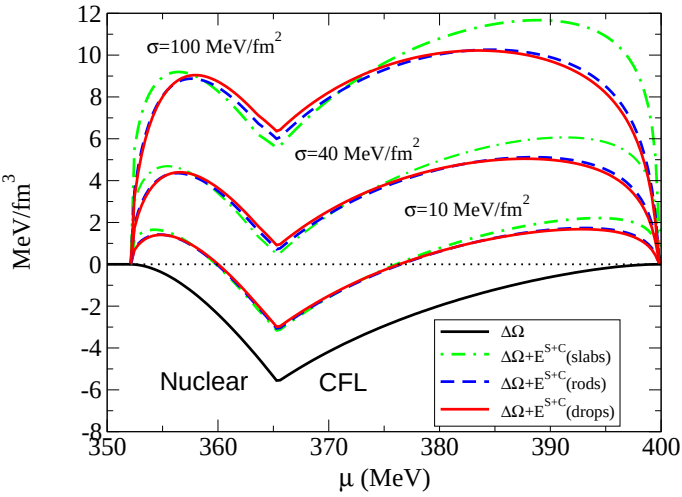

Fig. 8. The free energy difference between the mixed phase and the homogeneous neutral nuclear and CFL phases. In the lowest curve, the surface and Coulomb energy costs of the mixed phase are neglected, and the mixed phase therefore has the lower free energy. Other curves include surface and Coulomb energy for different values of $\sigma_{\rm QCD}$ and different mixed phase geometry. As $\sigma_{\rm QCD}$ increases, the surface and Coulomb price paid by the mixed phase increases.

of increasing density by a progression from drops to rods to slabs of CFL matter within nuclear matter followed by slabs to rods to drops of nuclear matter within CFL matter. This is the same progression of geometries seen in the inner crust of a neutron star [32] or in the mixed phase at a first-order phase transition between nuclear matter and unpaired quark matter [33] or hadronic kaon condensate [34]. We have also checked that for $\sigma_{\rm QCD} = 10$ and 40 MeV/fm^2, with the mixed phase geometry at any χ taken to be that favored, the sizes of regions of both phases (r_0 and its suitably defined counterpart) are always $\lesssim 6$ fm. In general, uniform regions of charge can only exist on length scales small compared to the Debye screening length. The Debye screening length in the quark and hadronic phase are typically of the size 5 to 10 fm [33]. When the size of the charged regions becomes comparable to the Debye screening length, it becomes important to account for spatial variations of the charge density. This will influence the surface and Coulomb energy estimates presented in Eq. (4.6). A detailed discussion of the importance of these finite-size effects is presented in Ref. [35].

For any given $\sigma_{\rm QCD}$, the mixed phase has lower free energy than homogeneous neutral CFL or nuclear matter wherever one of the curves in Fig. 8 for that $\sigma_{\rm QCD}$ is negative. We see that some of the mixed phase will

survive if $\sigma_{\rm QCD} \approx 10$ MeV/fm^2 while for $\sigma_{\rm QCD} \gtrsim 40$ MeV/fm^2 the mixed phase is not favored for any μ. This means that if the QCD-scale surface tension $\sigma_{\rm QCD} \gtrsim 40$ MeV/fm^2, a single sharp interface will be favored. The interface is characterized by a bipolar charge distribution, resulting in an intense electric field which ensures that the electric-charge chemical potential is continuous across it (see Ref. [23] for details).

5. Mass and radius of neutron stars

The equations that enforce the condition of hydrostatic equilibrium in compact stars, where general relativistic effects are important, are called the Tolman–Oppenheimer–Volkov (TOV) equations [36]. They are given by

$$\begin{aligned} \frac{dP}{dr} &= \frac{-G\ M(r)\ \varepsilon(P)}{r^2\ c^2}\left(1+\frac{P}{\varepsilon}\right)\ \left(1+\frac{4\pi r^3 P}{M(r)c^2}\right)\left((1-\frac{2GM(r)}{rc^2}\right)^{-1} \\ \frac{dM(r)}{dr} &= 4\pi^2\ \varepsilon(P)\,, \end{aligned} \tag{5.1}$$

where $P = P(r)$ and the equation of state specifies $\varepsilon(P)$, *i.e.*, the energy density as a function of the pressure, and $M(r)$ is the total energy enclosed within radius r. For a given central pressure, $P(r=0)$, the above equations can be easily integrated out to the surface of the star, where $P = 0$, to obtain the mass and radius of the object.

A family of stars all described by the same EoS can be obtained by parametrically varying the central pressure and repeating the procedure described above. Fig. 9 shows the mass–radius curve obtained in this way for two different nuclear equation of states. The curve labeled "Mean-Field" corresponds to the model described in Section 2 and the curve labeled APR is a microscopic many-body calculation, by Akmal, Pandharipande and Ravenhall, of the EoS using realistic nucleon–nucleon potentials [37]. The dashed lines labeled $R = R_s$ and $R = 1.52R_s$ (where $R_s = 2GM/c^2$ is Schwarzchild radius) are model-independent constraints that require all stable stars to be to their right. To the left of the line defined by $R = R_s$ the objects must be black holes since the event horizon is outside the object, to the left of the line defined by $R = 1.52R_s$ the star requires a very stiff EoS for which the speed of sound, $c_s = \sqrt{dP/d\varepsilon}$, exceeds the speed of light [38]. The last stable orbit around a neutron star is located at a radius $R = 3R_s$. In some accreting neutron star systems called QPO's (Quasi-Periodic Oscillators) there is observational evidence of the existence of such orbits. This implies that they exist outside the physical radius of the star. This constrains stars to lie to the left of the line defined by $R = 3R_s$. Finally, the accurate measurement of the neutron star mass in the Hulse–Taylor binary system (PSR 1913+16) introduces a further constraint which requires that the maximum

mass of the stars constructed using any model EoS be at least as large as 1.44 $M_\odot$ [39].

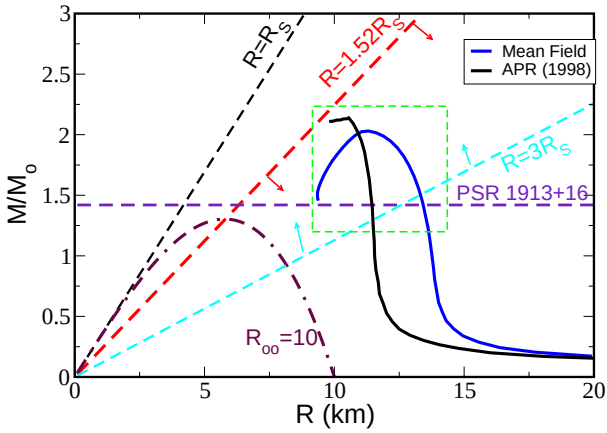

Fig. 9. Mass–radius relation for nuclear stars, where M_o is the mass of our sun.

The radius of the neutron star as inferred from a point far away (compared to R_s) is $R_\infty = R/\sqrt{1 - R_s/R}$ where R is the radius of the star, as inferred from the TOV equation. An accurate determination of R_∞ would greatly constrain the allowed region in the mass radius diagram. For example, a precise measurement of an R_∞ of 10 km constrains all stars to lie on the curve labeled $R_\infty = 10$ km in Fig. 9. The discovery of a nearby isolated neutron star which appears to emit nearly black-body radiation promises to provide valuable information about R_∞ [40]. Assuming that the object is emitting black-body radiation, a measurement of the photon energy flux F and the distance to the object d uniquely determine R_∞ as

$$R_\infty = d\sqrt{\frac{F}{\sigma_{\rm SB} T_\infty^4}}\,, \tag{5.2}$$

where $\sigma_{\rm SB}$ is the Stefan–Boltzmann constant and T_∞ is the temperature of the black-body spectrum inferred at infinity. In the case of RXJ 185635-3754, the X-ray spectrum is fit to good approximation by a black-body spectrum. The distance to this object $d \simeq 117$ pc [42, 43]. However, the optical and X-ray data cannot be reconciled with a single temperature black-body spectrum [41]. Consequently a stringent constraint of the form described by the $R_\infty = 10$ km curve is not yet possible [41, 43].

Phase transitions at high density generically result in an increase in the energy density of matter at a given pressure. We will loosely refer to this as softening. An EoS whose energy density (as a function of pressure) is on-average large compared to the nuclear EoS can be considered to be soft. A

larger energy density increases the gravitation attraction inside the compact object. Consequently, it will require higher central pressures to achieve hydrostatic equilibrium for a given mass of the compact object. However, with increasing pressure, the energy density increases rapidly in a soft EoS. The competition between matter pressure and gravity is heavily stacked in favor of gravity in a star with a soft EoS. This results in lower maximum masses and smaller radii.

This trend is shown in Fig. 10. The mass–radius relationship for a hybrid compact object containing nuclear matter at low density and pure quark matter at high density is shown (black curve labeled NQ). Other exotic possibilities like hyperons (NH), kaon condensation (NK) and phase transitions in which a mixed nuclear-quark phase is favored (NQM) have a similar effect on the mass–radius curve. Kaon condensation results in stars that are relatively compact while the hyperonic and the nuclear-quark mixed phase stars favor modestly larger maximum masses and radii. The rough estimate of the region of the M–R diagram which can be populated by exotic stars given the uncertainties in these models is also indicated by the dashed box. Mass and radius are integral quantities and are sensitive to the EoS over a wide range of densities. Therefore, in principle one requires a large number of different and simultaneous mass–radius measurements to directly infer the EoS. However, our knowledge of the nuclear properties at nuclear saturation density and nuclei provide valuable additional information. This is encoded

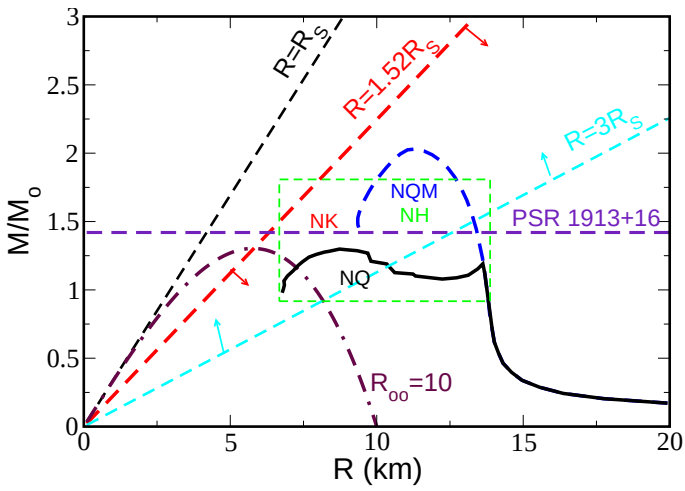

Fig. 10. Mass–radius relation for several exotic stars. The symbols NK, NH and NQM refer to locations where we expect the maximum masses of such stars to lie. They represent generic trends rather than precise locations. The mean-field EoS is employed to represent the nuclear part of the star.

in most realistic equations of state and lead to the generic trends described above. The accurate measurement of both the mass and radius of star will provide a very stringent constraint on the high density EoS. For example, the discovery of a compact object with a $R \lesssim 8$ km would provide strong support for the existence of novel phases inside neutron stars. On the other hand, the accurate measurement of neutron star mass $M \gtrsim 1.8\ M_\odot$ would support the absence of phase transitions. While neither of these hypothetical measurements will provide conclusive evidence, they will provide valuable guidance to the theoretical models of high-density matter.

6. Supernova neutrinos

Neutrinos play an important role in stellar evolution. By virtue of their weak interactions with matter, neutrinos provide a mechanism for energy loss from dense stellar interiors. In neutron stars neutrinos are responsible for most of the energy radiated from their birth in a supernova explosion through several thousand years of subsequent evolution. In this section we present an overview of some of the nuclear/particle physics issues that play a role in understanding the rate of propagation and production of neutrinos inside neutron stars. The calculation of these rates is of current interest since several research groups are embarking on large-scale numerical simulations of supernova and neutron star evolution [44–46]. Even moderate changes in the nuclear microphysics associated with the weak interaction rates at high density can impact macroscopic features that are observable. An understanding of the response of the strongly interacting nuclear medium to neutrinos and its impact on neutron star evolution promises to provide a means of probing the properties of the dense medium itself [47–49].

In this section we discuss neutrino interactions in dense matter containing nucleons and leptons and neutrino interactions in exotic new phases that are likely to occur in the dense inner core of the neutron star. We emphasize the generic aspects of the microphysics that affect the weak interaction rates and present supporting qualitative arguments (for a detailed account see Ref. [50]).

6.1. Neutrino interactions in nucleonic matter

It was realized over a decade ago that the effects due to degeneracy and strong interactions significantly alter the neutrino mean free paths and neutrino emissivities in dense matter [51–54]. However, it is only recently that detailed calculations have become available [55–65]. The scattering and absorption reactions that contribute to the neutrino opacity are

$$\begin{aligned} \nu_e + B &\rightarrow e^- + B', \qquad \bar{\nu}_e + B \rightarrow e^+ + B', \\ \nu_X + B &\rightarrow \nu_X + B', \qquad \nu_X + e^- \rightarrow \nu_X + e^-, \end{aligned} \tag{6.1}$$

where the scattering reactions are common to all neutrino species and the dominant source of opacity for the electron neutrinos is due to the charged-current reaction. The important neutrino producing reactions in the neutron star context are

$$\begin{aligned} e^- + p &\rightarrow n + \nu_e\,, \qquad & n &\rightarrow e^- + p + \bar{\nu}_e\,, \\ n + n &\rightarrow n + p + e^- + \bar{\nu}_e\,, & n + n &\rightarrow n + n + \nu_X + \bar{\nu}_X\,. \end{aligned} \tag{6.2}$$

The weak interaction rates for the reactions in Eq. (6.1) and Eq. (6.2) are modified in hot and dense matter because of many in-medium effects. The most important of these are:

(1) *Composition*: The rate for neutrino processes depends sensitively on the composition of the medium, which is itself sensitive to the nature of strong interactions. First, the different degeneracies of the different fermions determine the particle–hole response due to Pauli blocking. For example, a larger symmetry energy favors higher proton fractions. This directly impacts the weak rates because neutrinos couple differently to different baryonic species and because the Pauli and momentum-conservation restrictions on rates involving neutrons and protons are relaxed. Consequently, the net rates will depend on the individual concentrations.

(2) *In-medium dispersion relations*: At high density the single-particle dispersion relations are significantly modified from their non-interacting forms due to effects of strong interactions. Interacting matter features smaller effective baryon masses and energy shifts relative to non-interacting matter. This in turn affects the weak interaction rates primarily because it modifies the density of particle–hole states at the Fermi surface.

(3) *Correlations*: Low-energy neutrinos couple mainly to the long wavelength density and spin-density fluctuations of the strongly interacting nuclear plasma. Repulsive particle–hole interactions and Coulomb interactions generally result in a suppression of the weak interaction rates since they increase the energy cost associated with of such fluctuations. On the other hand, interactions can also result in low-lying collective excitations to which neutrinos can couple. This acts to increase the weak interaction rates at low energy. Both of these effects may be calculated using the Random Phase Approximation (RPA), in which particle–hole ring diagrams are summed to all orders. Model calculations [51,53–55,58,60,62–64] indicate that at high density the neutrino cross sections are suppressed relative to the case in which these effects are ignored. In addition, these correlations enhance the average energy transfer in neutrino-nucleon collisions. Improvements in determining many-body dynamic form factors and assessing the role of particle–particle interactions in dense matter at finite temperature are necessary before the full effects of many-body correlations may be ascertained.

The relative importance of the various effects described above on neutrino transport is only beginning to be studied systematically. As a first step, we will focus on effects due to modifications (1) through (3) above. To see how this is accomplished we start with a general expression for the differential cross section [55,62] for the processes shown in Eq. (6.1)

$$\frac{1}{V}\frac{d^3\sigma}{d^2\Omega_3 dE_3} = -\frac{G_{\rm F}^2}{128\pi^2}\frac{E_3}{E_1}\left[1-\exp\left(\frac{-q_0-(\mu_2-\mu_4)}{k_{\rm B}T}\right)\right]^{-1} \times(1-f_3(E_3))\ {\rm Im}\ (L^{\alpha\beta}\Pi^{\rm R}_{\alpha\beta})\,, \tag{6.3}$$

where the incoming neutrino energy is E_1, the outgoing lepton energy is E_3 and the energy transfer $q_0 = E_3 - E_1$. The factor $[1-\exp((-q_0-\mu_2+\mu_4)/k_{\rm B}T)]^{-1}$ maintains detailed balance for particle which are in thermal equilibrium at temperature T and in chemical equilibrium with chemical potentials μ_2 and μ_4, respectively. The final state blocking of the outgoing lepton is accounted for by the Pauli blocking factor $(1-f_3(E_3))$, where f_3 is the Fermi distribution function. The lepton tensor $L_{\alpha\beta}$ is given by

$$L^{\alpha\beta} = 8[2k^\alpha k^\beta + (k\cdot q)g^{\alpha\beta} - (k^\alpha q^\beta + q^\alpha k^\beta) \mp i\varepsilon^{\alpha\beta\mu\nu}k^\mu q^\nu]\,, \tag{6.4}$$

where k_μ is the incoming neutrino four-momentum and q_μ is the four-momentum transfer. In writing the lepton tensor, we have neglected the electron mass terms, since typical electron energies are of the order of a few hundred MeV.

The target–particle retarded polarization tensor is

$${\rm Im}\Pi^{\rm R}_{\alpha\beta} = \tanh\left(\frac{q_0+(\mu_2-\mu_4)}{2T}\right){\rm Im}\ \Pi_{\alpha\beta}\,, \tag{6.5}$$

where $\Pi_{\alpha\beta}$ is the time-ordered (or causal) polarization and is given by

$$\Pi_{\alpha\beta}(q) = -i\int\frac{d^4p}{(2\pi)^4}{\rm Tr}\ [T(S_2(p)\Gamma_\alpha S_4(p+q)\Gamma_\beta)]\,. \tag{6.6}$$

The Greens' functions $S_i(p)$ (the index i labels particle species) describe the propagation of baryons at finite density and temperature [55]. The current operator Γ_μ is γ_μ for the vector current and $\gamma_\mu\gamma_5$ for the axial current. Effects of strong and electromagnetic correlations may be included by calculating the RPA polarization tensor

$$\Pi^{\rm RPA} = \Pi + \Pi^{\rm RPA}D\Pi\ , \tag{6.7}$$

where D denotes the strong interaction matrix (see Ref. [62] for more details).

Neutrino mean free path, which is inversely related to the cross section per unit volume, calculated in relativistic RPA is shown in Fig. 11. The model employed incorporates interactions via σ, ω, and ρ exchange as in Walecka model [55,62]. It is supplemented by pion exchange and a repulsive contact term, whose strength is parameterized by a constant $g' \simeq 0.6$ to account for short-range spin–isospin correlations. The results indicate that RPA corrections are most significant in the spin–isospin channel and that low-temperature correlation can suppress the cross section by a factor of two or more. This is because, in the Fermi-gas limit, the axial-vector response

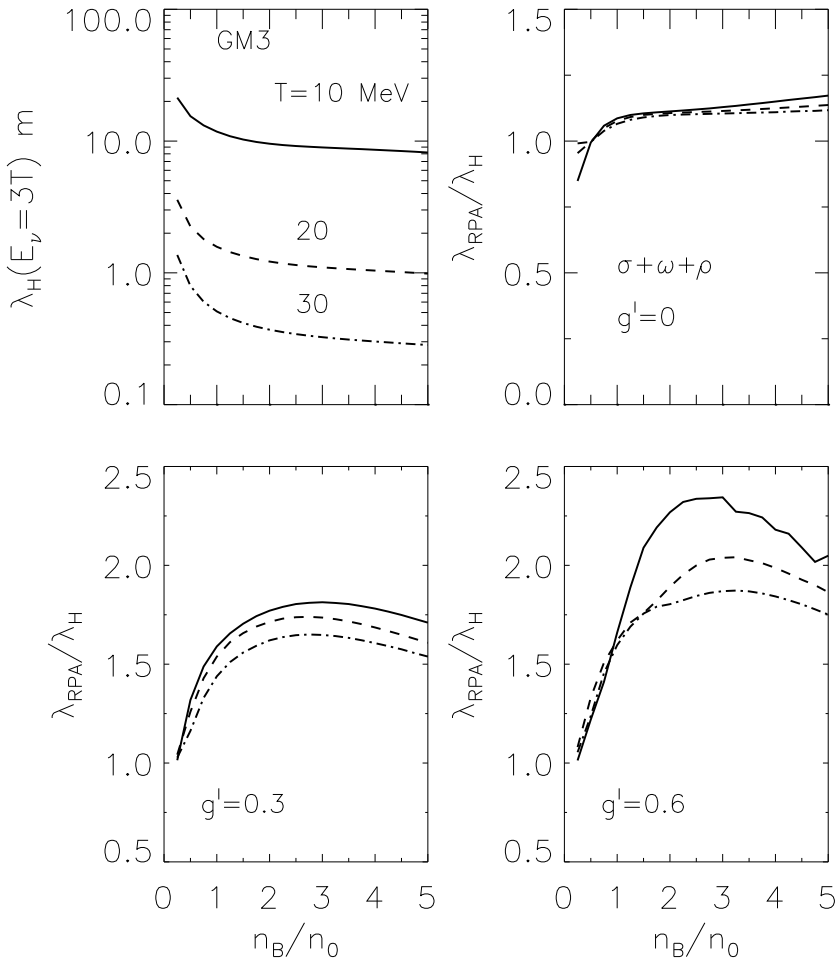

Fig. 11. Neutrino mean free paths in dense stellar matter containing neutron, protons and electrons calculated in the relativistic RPA ($\lambda_{\rm RPA}$) and normalized to those computed in the mean field or Hartree approximation ($\lambda_{\rm H}$) [62].

of medium makes a contribution that is roughly three times larger than the vector response [53]. Quantitative aspects of the suppression depend on the details of the model employed. Nonetheless, we note that most model studies thus far indicate similar suppression factors.

6.2. Neutrino interactions in novel phases

In this section we explore how phase transitions impact the weak interaction rates. As discussed in earlier sections, novel phases of baryonic matter are expected to occur at densities accessible in neutron stars. These new phases include pion condensation, kaon condensation, hyperons and quark matter. An understanding of how these phases might influence neutrino propagation and emission is necessary if we are to inquire if these phase transitions even occur inside neutron stars. To illustrate how they neutrino rates we consider three specific examples of phase transitions: (1) generic first-order transitions; (2) superconducting quark matter and (3) color-flavor-locked superconducting quark matter.

6.2.1. Inhomogeneous phases: effects of first-order transitions

First-order phase transitions in neutron stars can result in the formation of heterogeneous phases in which a positively-charged nuclear phase coexists with a negatively-charged new phase which is favored at higher densities [31]. This is a generic feature of first-order transitions in matter with two conserved charges. In the neutron star context these correspond to baryon number and electric-charge. Reddy, Bertsch and Prakash [66] have studied the effects of inhomogeneous phases on ν-matter interactions. Based on simple estimates of the surface tension between nuclear matter and the exotic phase, typical droplet sizes range from 5–15 fm [67], and interdroplet spacings are several times larger. The propagation of neutrinos whose wavelength is greater than the typical droplet size and less than the interdroplet spacing, *i.e.*, 2 MeV $\leq E_\nu \leq$ 40 MeV, will be greatly affected by the heterogeneity of the mixed phase, as a consequence of the coherent scattering of neutrinos from the droplet.

The Lagrangian that describes the neutral-current coupling of neutrinos to the droplet is

$$\mathcal{L}_{\rm W} = \frac{G_{\rm F}}{2\sqrt{2}}\, \bar{\nu}\gamma_\mu(1-\gamma_5)\nu\; J_D^\mu\,, \tag{6.8}$$

where J_D^μ is the neutral weak current carried by the droplet and $G_{\rm F} = 1.166\times10^{-5}$ GeV^{-2} is the Fermi weak coupling constant. For non-relativistic droplets, J_D^μ has only a time-like component, $\rho_{\rm W}(x)$, where $\rho_{\rm W}$ is the excess weak charge density in the droplet. The total weak charge enclosed in a

droplet of radius r_d is $N_{\rm W} = \int_0^{r_d} d^3x\ \rho_{\rm W}(x)$ and the associated form factor is

$$F(q) = (1/N_{\rm W}) \int_0^{r_d} d^3x\ \rho_{\rm W}(x)\ \sin qx/qx\,. \tag{6.9}$$

The differential cross section for neutrinos scattering from an isolated droplet is then

$$\frac{d\sigma}{d\cos\theta} = \frac{E_\nu^2}{16\pi} G_{\rm F}^2 N_{\rm W}^2 (1+\cos\theta) F^2(q)\,. \tag{6.10}$$

In the above equation, E_ν is the neutrino energy and θ is the scattering angle. Since the droplets are massive, we consider only elastic scattering for which the magnitude of the three-momentum transfer is $q = \sqrt{2}E_\nu(1-\cos\theta)$.

We must embed the droplets in the medium to evaluate the neutrino transport parameters. The droplet radius r_d and the inter-droplet spacing are determined by the interplay of surface and Coulomb energies. In the Wigner–Seitz approximation, the unit-cell radius is $R_{\rm W} = (3/4\pi N_D)^{1/3}$ where the droplet density is N_D. Multiple droplet scattering cannot be neglected for $E_\nu \lesssim 1/R_{\rm W}$. The effects of other droplets is to cancel scattering in the forward direction, because the interference is destructive except at exactly zero degrees, where it only produces a change in the index of refraction of the medium.

These effects are usually incorporated by multiplying the differential cross section Eq. (6.10) by the static form factor of the medium. The static form factor, defined in terms of the radial distribution function of the droplets, $g(r)$, is

$$S(q) = 1 + N_D \int d^3r \exp i\vec{q}\cdot\vec{r}\ [g(r)-1]\,. \tag{6.11}$$

The droplet correlations, which determine $g(r)$, arise due to the Coulomb force and are measured in terms of the dimensionless Coulomb number $\Gamma = Z^2e^2/(8\pi R_{\rm W} kT)$. Due to the long-range character of the Coulomb force, the role of screening, and the finite droplet size, $g(r)$ cannot be computed analytically. We use a simple form for the radial distribution function $g(r) = \theta(r - R_{\rm W})$. This choice for $g(r)$ is equivalent to subtracting, from the weak charge density $\rho_{\rm W}$, a uniform density which has the same total weak charge $N_{\rm W}$ as the matter in the Wigner–Seitz cell. Thus, effects due to $S(q)$ may be incorporated by replacing the form factor $F(q)$ by

$$\tilde{F}(q) = F(q) - 3\ \frac{\sin qR_{\rm W} - (qR_{\rm W})\cos qR_{\rm W}}{(qR_{\rm W})^3}\,. \tag{6.12}$$

The neutrino–droplet differential cross section per unit volume then follows:

$$\frac{1}{V}\frac{d\sigma}{d\cos\theta} = N_D \ \frac{E_\nu^2}{16\pi} G_{\rm F}^2 N_{\rm W}^2 (1+\cos\theta)\tilde{F}^2(q)\,. \tag{6.13}$$

Note that even for small droplet density N_D, the factor $N_{\rm W}^2$ acts to enhance the droplet scattering since, as we shall see below $N_{\rm W} \sim 800$.

To quantify the importance of droplets as a source of opacity, we compare with the standard scenario in which matter is uniform and composed of neutrons. The dominant source of opacity is then due to scattering from thermal fluctuations and, in the non-relativistic limit Eq. (6.3) reduces to

$$\frac{1}{V}\frac{d\sigma}{d\cos\theta} = \frac{3G_{\rm F}^2\ E_\nu^2}{16\pi}\left[c_V^2(1+\cos\theta) + (3-\cos\theta)c_A^2\right] n_n \left[\frac{k_{\rm B}T}{E_{{\rm F}n}}\right], \tag{6.14}$$

where c_V and c_A are respectively the vector and axial coupling constants of the neutron, n_n is the neutron number density, $E_{{\rm F}n} = k_{{\rm F}n}^2/2M_n$ is the neutron Fermi energy and T is the matter temperature [53]. The transport cross sections that are employed in studying the diffusive transport of neutrinos in the core of a neutron star are differential cross sections weighted by the angular factor $(1-\cos\theta)$. The transport mean free path, $\lambda(E_\nu)$, for a given neutrino energy E_ν is given by

$$\frac{1}{\lambda(E_\nu)} = \frac{\sigma_T(E_\nu)}{V} = \int d\cos\theta\ (1-\cos\theta)\left[\frac{1}{V}\frac{d\sigma}{d\cos\theta}\right]. \tag{6.15}$$

Models of first-order phase transitions in dense matter provide the weak charge and form factors of the droplets and permit the evaluation of ν-droplet scattering contributions to the opacity of the mixed phase. We consider two models, namely the first-order kaon condensate and the quark–hadron phase transition. The neutrino mean free paths in the mixed phase are shown in the left and right panels of Fig. 12, respectively. The results are shown for the indicated values of the baryon density n_B and temperature T, where the model predicts a mixed phase exists. The kaon droplets are characterized by radii $r_d \approx 7$ fm and inter-droplet spacings $R_{\rm W} \approx 20$ fm, and enclose a net weak charge $N_{\rm W} \approx 700$. The quark droplets are characterized by $r_d \approx 5$ fm, and $R_{\rm W} \approx 11$ fm, and an enclosed excess weak charge $N_{\rm W} \approx 850$. For comparison, the neutrino mean free path in uniform neutron matter at the same n_B and T are also shown. The typical neutrino energy for neutrino in thermal equilibrium is given by $E_\nu \approx \pi T$ (the factor π here is just a convenient approximation). For these energies, it is apparent that there is a large coherent scattering-induced reduction in the mean free path. At much lower energies, the interdroplet correlations tend to screen the weak charge of the droplet, and at higher energies the coherence is attenuated by the droplet form factor.

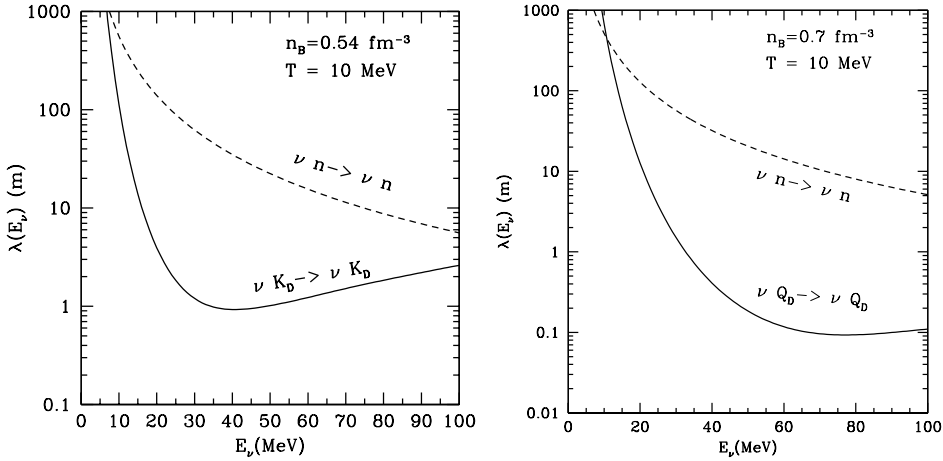

Fig. 12. Neutrino mean free paths as a function of neutrino energy. Solid lines are for matter in a mixed phase containing kaons (left panel) and quarks (right panel), and dashed curves are for uniform matter.

The large reduction in neutrino mean free path found here implies that a mixed phase will cool significantly slower than homogeneous matter. Consequently, the observable neutrino luminosity at late times might be affected, as it is driven by the transport of energy from the deep interior.

6.2.2. Effects of quark superconductivity

As discussed previously, recent theoretical works [18, 19] suggest that quarks form Cooper pairs in medium, a natural consequence of attractive interactions destabilizing the Fermi surface. Model calculations, mostly based on four-quark effective interactions (Nambu–Jona-Lasinio-like models), predict the restoration of spontaneously broken chiral symmetry through the onset of color superconductivity at relatively low temperatures. They predict an energy gap of $\Delta \sim 100$ MeV for a typical quark chemical potential of $\mu \sim 400$ MeV. As in BCS theory, the gap will weaken for $T > 0$, and at some critical temperature $T_{\rm c}$ there is a (second-order) transition to a normal or unpaired quark–gluon plasma. During cooling from an initial temperature in excess of $T_{\rm c}$, the formation of a gap in the fermion excitation spectrum in quark matter will influence various transport properties of the system. Carter and I have studied its influence on the transport of neutrinos [68].

The differential neutrino scattering cross section per unit volume in an infinite and homogeneous system of relativistic fermions as calculated in linear response theory is given by Eq. (6.3). The medium is characterized by the quark polarization tensor $\Pi_{\alpha\beta}$. In the case of free quarks, each flavor

contributes a term of the form

$$\Pi_{\alpha\beta}(q) = -i\mathrm{Tr_c}\int \frac{d^4p}{(2\pi)^4}\mathrm{Tr}\left[S_0(p)\Gamma_\alpha S_0(p+q)\Gamma_\beta\right], \tag{6.16}$$

where $S_0(p)$ is the free quark propagator. At finite chemical potential and temperature the quark propagator is given by

$$S_0(p)^{bg}_{af} = i\delta^b_a\delta^g_f\left(\frac{\Lambda^+(p)}{p_0^2-E_p^2}+\frac{\Lambda^-(p)}{p_0^2-\bar{E}_p^2}\right)(p_\mu\gamma^\mu-\mu\gamma_0). \tag{6.17}$$

This is written in terms of the particle and anti-particle projection operators $\Lambda^+(p)$ and $\Lambda^-(p)$ respectively, where $\Lambda^\pm(p) = (1\pm\gamma_0\vec{\gamma}\cdot\hat{p})/2$. The excitation energies are simply $E_p = |\vec{p}|-\mu$ for massless quarks and $\bar{E}_p = |\vec{p}|+\mu$ for massless anti-quarks. The outer trace in Eq. (6.16) is over color and simplifies to 3. The inner trace is over spin, and the Γ_α are the neutrino-quark vertex functions. Specifically, the vector polarization is computed by choosing $(\Gamma_\alpha,\Gamma_\beta) = (\gamma_\alpha,\gamma_\beta)$. The axial and mixed vector–axial polarizations are similarly obtained from $(\Gamma_\alpha,\Gamma_\beta) = (\gamma_\alpha\gamma_5,\gamma_\beta\gamma_5)$ and $(\Gamma_\alpha,\Gamma_\beta) = (\gamma_\alpha,\gamma_\beta\gamma_5)$, respectively.

The free quark propagators in Eq. (6.16) are modified in a superconducting medium. In calculating these effects, we will consider the simplified case of QCD with two quark flavors which obey $\mathrm{SU(2)_L}\otimes\mathrm{SU(2)_R}$ flavor symmetry, given that the light u and d quarks dominate low-energy phenomena. Furthermore we will assume that, through some unspecified effective interactions, quarks pair in a manner analogous to the BCS mechanism [17]. The relevant consequences of this are the restoration of chiral symmetry (hence all quarks are approximately massless) and the existence of an energy gap at zero temperature, Δ_0. As discussed earlier in section 3.4, this superconducting phase is called the 2SC phase. The approximate temperature dependence of the gap is taken from BCS theory

$$\Delta(T) = \Delta_0\sqrt{1-\left(\frac{T}{T_\mathrm{c}}\right)^2}, \tag{6.18}$$

where the critical temperature $T_\mathrm{c}\simeq 0.57\Delta_0$; this relation has been shown to hold for perturbative QCD and is thus a reasonable assumption for non-perturbative physics. Since the scalar diquark (in the $\bar{\mathbf{3}}$ color representation) is the most attractive channel, we consider the anomalous propagator [69]

$$\begin{aligned} F(p)_{abfg} &= \langle q^T_{fa}(p)C\gamma_5 q_{gb}(-p)\rangle \\ &= -i\varepsilon_{ab3}\varepsilon_{fg}\Delta\left(\frac{\Lambda^+(p)}{p_0^2-\xi_p^2}+\frac{\Lambda^-(p)}{p_0^2-\bar{\xi}_p^2}\right)\gamma_5\ C. \end{aligned} \tag{6.19}$$

Here, a, b are color indices, f, g are flavor indices, ε_{abc} is the usual antisymmetric tensor and we have conventionally chosen 3 to be the condensate color. The quasi-particle energy is $\xi_p = \sqrt{(|\vec{p}| - \mu)^2 + \Delta^2}$, and for the antiparticle $\bar{\xi}_p = \sqrt{(|\vec{p}| + \mu)^2 + \Delta^2}$. This propagator is also antisymmetric in flavor and spin, with $C = -i\gamma_0\gamma_2$ being the charge conjugation operator.

The color bias of the condensate forces a splitting of the normal quark propagator into colors transverse and parallel to the diquark. Quarks of color 3, parallel to the condensate in color space, will be unaffected and propagate freely. Their response is characterized by the polarization tensor given in Eq. (6.16), but without the trace over color space since it involves only quarks of one color. On the other hand, transverse quark colors 1 and 2 participate in the diquark and thus their quasi-particle propagators are given as

$$S(p)^{bg}_{af} = i\delta^b_a\delta^g_f \left(\frac{\Lambda^+(p)}{p_o^2 - \xi_p^2} + \frac{\Lambda^-(p)}{p_o^2 - \bar{\xi}_p^2} \right) (p_\mu\gamma^\mu - \mu\gamma_0) \,. \tag{6.20}$$

The appearance of an anomalous propagator in the superconducting phase indicates that the polarization tensor gets contributions from both the normal quasi-particle propagators Eq. (6.20) and anomalous propagator Eq. (6.19). Thus, to order $G_{\rm F}^2$, Eq. (6.16) is replaced with the two contributions corresponding to the normal and anomalous diagrams and is given by

$$\begin{aligned} \Pi_{\alpha\beta}(q) \;=\; & -i\int \frac{d^4p}{(2\pi)^4} \{ \mathrm{Tr}\,[S_0(p)\Gamma_\alpha S_0(p+q)\Gamma_\beta] \\ & + 2\mathrm{Tr}\,[S(p)\Gamma_\alpha S(p+q)\Gamma_\beta] \\ & + 2\mathrm{Tr}\,[F(p)\Gamma_\alpha \bar{F}(p+q)\Gamma_\beta] \} \,. \end{aligned} \tag{6.21}$$

The $S(p)$-$F(p)$ mixed terms vanish and the remaining trace is over spin, as the color trace has been performed giving the factors of 2.

For neutrino scattering we must consider vector, axial, and mixed vector–axial channels, all summed over flavors. The full polarization, to be used in evaluating Eq. (6.3), may be written

$$\Pi_{\alpha\beta} = \sum_f \left[(c_V^f)^2 \Pi^V_{\alpha\beta} + (c_A^f)^2 \Pi^A_{\alpha\beta} - 2c_V^f c_A^f \Pi^{VA}_{\alpha\beta} \right] \,. \tag{6.22}$$

The coupling constants for up quarks are $c_V^u = \frac{1}{2} - \frac{4}{3}\sin^2\theta_{\rm W}$ and $c_A^u = \frac{1}{2}$, and for down quarks, $c_V^d = -\frac{1}{2} + \frac{2}{3}\sin^2\theta_{\rm W}$ and $c_A^d = -\frac{1}{2}$, where $\sin^2\theta_{\rm W} = 0.23$ is the Weinberg angle.

The differential cross section, Eq. (6.3), and the total cross section are obtained by integrating over all neutrino energy transfers and/or angles. Results for the neutrino mean free path, $\lambda = V/\sigma$, are shown in Fig. 13 as a function of incoming neutrino energy E_ν (for ambient conditions of $\mu = 400$ MeV and $T = 30$ MeV). They show the same energy dependence found previously for free relativistic and degenerate fermion matter [61]; $\lambda \propto 1/E_\nu^2$ for $E_\nu \gg T$ and $\lambda \propto 1/E_\nu$ for $E_\nu \ll T$. The results indicate that this energy dependence is not modified by the presence of a gap when $\Delta \sim T$. Thus, the primary effect of the superconducting phase is a much larger mean free path. This is consistent with the suppression found in the vector-longitudinal response function, Π_{00}^V, which dominates the polarization sum Eq. (6.22), at $q_0 < q$.

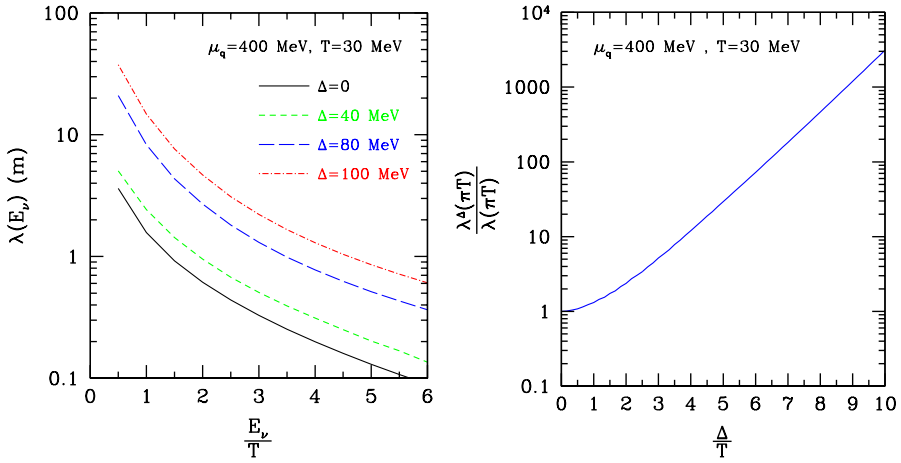

Fig. 13. Left panel: Neutrino mean free path as a function of neutrino energy E_ν. Right panel: Neutrino mean free paths for $E_\nu = \pi T$ as a function of $\Delta(T)/T$. These results are virtually independent of temperature for $T \lesssim 50$ MeV. λ^Δ and Λ denote the mean free paths in the superconducting and normal phases, respectively.

6.2.3. Neutrino interactions with collective excitations (Goldstone modes)

The discussion in the preceding section assumed that there were no low energy collective excitations to which the neutrinos could couple. As discussed in Sec. 3.4, this is true in the two-flavor superconducting (2SC) phase of quark matter. For three flavors and when the strange quark mass is negligible compared to the chemical potential, the ground state is characterized by pairing that involves all nine quarks in a pattern that locks flavor and color [21]. Naively we can expect significant differences in the weak interaction rates between the normal and the CFL phases of quark matter since

the latter is characterized by a large gap in the quark excitation spectrum. However, as detailed in Sec. 3.4, diquark condensation in the CFL phase breaks both baryon number and chiral symmetries. The Goldstone bosons that arise as a consequence introduce low-lying collective excitations to the otherwise rigid state. Thus, unlike in the normal phase where quark excitations near the Fermi surface provide the dominant contribution to the weak interaction rates, in the CFL phase it is the dynamics of the low-energy collective states– the Goldstone bosons –that are relevant. Neutrino interactions with Goldstone modes have been recently investigated by Jaikumar *et al.* [70] and Reddy *et al.* [71].

There are several articles that describe in detail the effective theory for Goldstone modes in CFL quark matter [22]. We will not review them here except to note that it is possible to parameterize low energy excitations about the SU(3) symmetric CFL ground state in terms of the two fields $B = H/\sqrt{24}f_H$ and $\Sigma = \exp 2i(\lambda \cdot \pi/f_\pi + \eta'/f_A)$. The B fields represent Goldstone modes of broken baryon number H. The Σ field of broken chiral symmetry, *i.e.*, the pseudo-scalar octet of Goldstone modes π, and the pseudo-Goldstone boson η'.

The massless Goldstone boson associated with spontaneous breaking of $\mathrm{U}(1)_B$ couples to the weak neutral current. This is because the weak isospin current contains a flavor singlet component. Although neutrinos couple to the flavor octet of Goldstone bosons, it turns out that the neutrino mean free path is mostly determined by processes involving the massless baryon number Goldstone mode [71]. For this reason, we focus our attention on these latter processes. The amplitude for processes involving the $\mathrm{U}(1)_B$ Goldstone boson H and the neutrino neutral current is given by [71]

$$A_{H\nu\bar{\nu}} = \frac{4}{\sqrt{3}}\, G_{\mathrm{F}}\; f_H\; \tilde{p}_\mu\; j_Z^\mu\,, \tag{6.23}$$

where $\tilde{p}_\mu = (E, v^2\vec{p})$ is the modified four momentum of the Goldstone boson and $v = c/\sqrt{3}$ is its velocity [71]. The decay constants for the $\mathrm{U}(1)_B$ and the pseudo-scalar octet of Goldstone modes have also been computed in earlier work [22] and are given by $f_H^2 = 3\mu^2/8\pi^2$ and $f_\pi^2 = (21 - 8\ln 2)\mu^2/36\pi^2$, respectively.

The neutrino mean free path due to the reaction $\nu \to H\nu$ can be calculated analytically and is given by

$$\frac{1}{\lambda_{\nu\to H\nu}(E_\nu)} = \frac{256}{45\pi}\left[\frac{v(1-v)^2(4+v)}{4\;(1+v)^2}\right]\; G_{\mathrm{F}}^2\; f_H^2 E_\nu^3\,. \tag{6.24}$$

Neutrinos of all energies can absorb a thermal mode and scatter into either a final state neutrino by neutral current processes like $\nu + H \to \nu$ and $\nu + \pi^0 \to \nu$ or via the charged-current reaction into a final state electron by the process $\nu_e + \pi^- \to e^-$. These processes are temperature dependent, since they are proportional to the density of Goldstone modes in the initial state. The mean free path due to these processes, which we collectively refer to as Cerenkov absorption, can be computed. Reactions involving the H boson dominate over other Cerenkov absorption processes due to their larger population and stronger coupling to the neutral current [71]. For this case we find the neutrino mean free path is given by

$$\begin{aligned} \frac{1}{\lambda_{\nu H\to\nu}(E_\nu)} &= F(v,\gamma) G_{\rm F}^2 \; f_H^2 \; E_\nu^3 \\ F(v,\gamma) &= \frac{128}{3\pi}\left[\frac{v\;(1+v)^2}{(1-v)}\right]\left[g_2(\gamma) + \frac{2v}{(1-v)} g_3(\gamma) - \frac{(1+v)}{(1-v)} g_4(\gamma)\right] , \end{aligned} \tag{6.25}$$

where $\gamma = 2vE_\nu/(1-v)k_{\rm B}T$ and the integrals $g_n(\gamma)$ are defined by

$$g_n(\gamma) = \int_0^1 dx \; \frac{x^n}{\exp(\gamma x) - 1} . \tag{6.26}$$

In contrast to processes involving the emission or absorption of the Goldstone modes by neutrinos, the usual scattering process involves the coupling of the neutrino current to two mesons. The amplitude for these processes vanishes for the H meson and is suppressed by the factor p/f_π where p is the mode momentum for the flavor octet Goldstone modes. Fig. 14 shows the contribution of all Goldstone boson–neutrino processes contributing to the neutrino mean free path in the CFL phase, including the dominant contribution arising from processes involving the massless mode.

It is interesting to note that the existence of one massless Goldstone mode compensates for the large gap in the particle–hole excitation spectrum. The contrast between the findings of the previous section where no low energy Goldstone modes coupled to neutrinos to those presented here is striking. The mean free path in the CFL phase is surprisingly similar to that in normal non-superconducting quark phase.

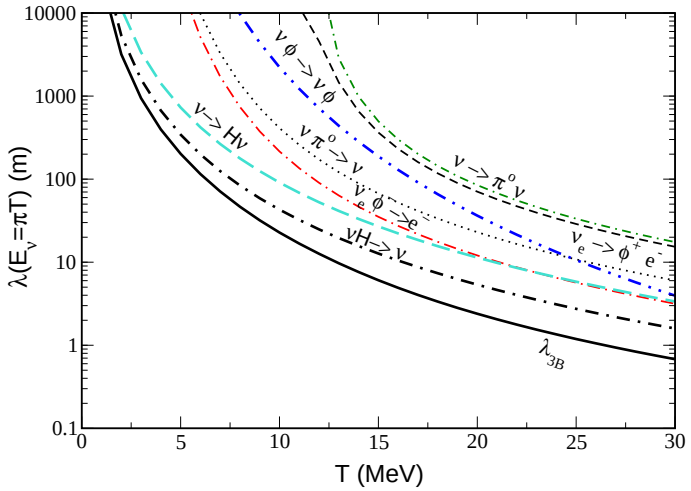

Fig. 14. Neutrino mean free path in a CFL meson plasma as a function of temperature. The neutrino energy $E_\nu = \pi T$ and is characteristic of a thermal neutrino. λ_{3B} is the total contribution of Cerenkov (absorption and emission) processes to the neutrino mean free path [71] and ϕ refers collectively to the octet of Goldstone modes.

7. Conclusions

Neutron stars are excellent laboratories to study possible phase transitions at high baryon density. We have attempted to provide a glimpse of the rich phenomena that may arise if such transitions were to occur inside these compact objects. The real challenge lies in being able to identify those characteristics of the phase transitions that will uniquely affect observable aspects of the neutron star structure and evolution. The structural properties of the star depend on the EoS of high-density matter. Generically, we found that phase transitions result in softening of the high-density EoS. In this case, the maximum mass and radius of neutron stars are lowered.

Neutrino production and propagation in dense matter directly impact neutron stars thermal evolution. The presence of novel phases at high density influences the low-energy weak interaction rates. For specific examples considered in this article we found that the rates could be either greatly enhanced or reduced. In some instances, the neutrino rates are left unchanged, albeit via novel compensating mechanisms. The theory of core collapse supernova evolution, and neutron star cooling, combined with future observations of supernova neutrinos and multi-wavelength photons from neutron stars has the potential to probe the inner core of these remarkable compact objects.

I would like to thank George Bertsch, Greg Carter, Mark Alford, David Kaplan, Jim Lattimer, Jose Pons, Madappa Prakash, Krishna Rajagopal, Mariusz Sadzikowski, Andrew Steiner, Motoi Tachibana and Frank Wilczek for enjoyable collaborations. The materials presented here are the results of these collaborations over the past four years. Special thanks are due to Dick Silbar for a careful reading of the manuscript and several valuable suggestions. This work is supported in part by funds provided by the U.S. Department of Energy (D.O.E.) under cooperative research agreement DF-FC02-94ER40818 and the D.O.E. contract W-7405-ENG-36.

REFERENCES

[1] D. Blaschke, N.K. Glendenning, A. Sedrakian, Physics of Neutron Star Interiors. Proceedings, Ect International Workshop, Nsi'00, Trento, Italy, June 19–July 6, (2000), *Lect. Notes Phys.* **578**, (2001).

[2] J.D. Walecka, *Ann. Phys.* **83**, 491 (1974).

[3] B.D. Serot, J.D. Walecka, *Adv. Nucl. Phys.* **16**, 1 (1986).

[4] J. Boguta, A.R. Bodmer, *Nucl. Phys.* **A292**, 413 (1977).

[5] N.K. Glendenning, *Compact Stars, Nuclear Physics, Particle Physics and General Relativity*, Springer-Verlag, New York 1997.

[6] D.J. Millener, C.B. Dover, A. Gal, *Phys. Rev.* **C38**, 2700 (1988).

[7] N.K. Glendenning, S.A. Moszkowski, *Phys. Rev. Lett.* **67**, 2414 (1991).

[8] C.J. Batty, E. Friedman, A. Gal, *Phys. Rep.* **287**, 385 (1997).

[9] E. Friedman, A. Gal, C.J. Batty, *Nucl. Phys.* **A579**, 518 (1994).

[10] A.B. Migdal, *Rev. Mod. Phys.* **50**, 107 (1978).

[11] D.B. Kaplan, A.E. Nelson, *Phys. Lett.* **B175**, 57 (1986).

[12] A. Ramos, J. Schaffner-Bielich, J. Wambach, *Lect. Notes Phys.* **578**, 175 (2001).

[13] J. Carlson, H. Heiselberg, V.R. Pandharipande, *Phys. Rev.* **C63**, 017603 (2001).

[14] B. Freedman, L.D. McLerran, *Phys. Rev.* **D17**, 1109 (1978).

[15] E.S. Fraga, R.D. Pisarski, J. Schaffner-Bielich, *Phys. Rev.* **D63**, 121702 (2001).

[16] A.R. Bodmer, *Phys. Rev.* **D4**, 1601 (1971); E. Witten, *Phys. Rev.* **D30**, 272 (1984).

[17] J. Bardeen, L.N. Cooper, J.R. Schrieffer, *Phys. Rev.* **108**, 1175 (1957).

[18] B.C. Barrois, *Nucl. Phys.* **B129**, 390 (1977). S.C. Frautschi: In *Workshop on Hadronic Matter at Extreme Energy Density*, Erice, Italy 1978.

[19] M.G. Alford, K. Rajagopal, F. Wilczek, *Phys. Lett.* **B422**, 247 (1998); R. Rapp, T. Schafer, E.V. Shuryak, M. Velkovsky, *Phys. Rev. Lett.* **81**, 53 (1998).

[20] K. Rajagopal, F. Wilczek, `hep-ph/0011333`; M.G. Alford, *Ann. Rev. Nucl. Part. Sci.* **51**, 131 (2001).

[21] M.G. Alford, K. Rajagopal, F. Wilczek, *Nucl. Phys.* **B537**, 443 (1999).

[22] R. Casalbuoni, R. Gatto, *Phys. Lett.* **B464**, 111 (1999); D.T. Son, M.A. Stephanov, *Phys. Rev.* **D61**, 074012 (2000); Erratum, *ibid.* **D62**, 059902 (2000); D.K. Hong, T. Lee, D. Min, *Phys. Lett.* **B477**, 137 (2000); C. Manuel, M.H. Tytgat, *Phys. Lett.* **B479**, 190 (2000); M. Rho, E. Shuryak, A. Wirzba, I. Zahed, *Nucl. Phys.* **A676**, 273 (2000); K. Zarembo, *Phys. Rev.* **D62**, 054003 (2000); S.R. Beane, P.F. Bedaque, M.J. Savage, *Phys. Lett.* **B483**, 131 (2000); D.K. Hong, *Phys. Rev.* **D62**, 091501 (2000); C. Manuel, M.H. Tytgat, *Phys. Lett.* **B501**, 200 (2001).

[23] M.G. Alford, K. Rajagopal, S. Reddy, F. Wilczek, *Phys. Rev.* **D64**, 074017 (2001).

[24] M.G. Alford, J. Berges, K. Rajagopal, *Nucl. Phys.* **B558**, 219 (1999).

[25] M. Buballa, M. Oertel, *Nucl. Phys.* **A703**, 770 (2002).

[26] P.F. Bedaque, T. Schafer, *Nucl. Phys.* **A697**, 802 (2002).

[27] D.B. Kaplan, S. Reddy, *Phys. Rev.* **D65**, 054042 (2002).

[28] K. Rajagopal, F. Wilczek, *Phys. Rev. Lett.* **86**, 3492 (2001).

[29] A.W. Steiner, S. Reddy, M. Prakash, `hep-ph/0205201`, to appear in *Phys. Rev.* **D**.

[30] C. Manuel, K. Rajagopal, *Phys. Rev. Lett.* **88**, 042003 (2002).

[31] N.K. Glendenning, *Phys. Rev.* **D46**, 1274 (1992).

[32] D.G. Ravenhall, C.J. Pethick, J.R. Wilson, *Phys. Rev. Lett.* **50**, 2066 (1983); D.G. Ravenhall, C.J. Pethick, *Annu. Rev. Nucl. Part. Sci.* **45**, 429 (1995).

[33] H. Heiselberg, C.J. Pethick, E.F. Staubo, *Phys. Rev. Lett.* **70**, 1355 (1993).

[34] N.K. Glendenning, J. Schaffner-Bielich, *Phys. Rev. Lett.* **81**, 4564 (1998).

[35] T. Norsen, S. Reddy, *Phys. Rev.* **C63**, 065804 (2001).

[36] J.R. Oppenheimer, G.M. Volkoff, *Phys. Rev.* **55**, 374 (1939).

[37] A. Akmal, V.R. Pandharipande, D.G. Ravenhall, *Phys. Rev.* **C58**, 1804 (1998).

[38] S. Weinberg, *Gravitation and Cosmology; Principles and Applications of the General Theory of Relativity*, New York: John Wiley & Sons 1972.

[39] R.A. Hulse, J.H. Taylor, *Astrophys. J.* **195**, L51 (1975).

[40] F.M. Walter, S.J. Wolk, R. Neuhauser, *Nature* **379**, 233 (1996).

[41] J.A. Pons, F.M. Walter, J.M. Lattimer, M. Prakash, R. Neuhauser, P. An, *Astrophys. J.* **564**, 981 (2002).

[42] D.L. Kaplan, M.H. van Kerkwijk, J. Anderson, `astro-ph/0111174`.

[43] F.M. Walter, J. Lattimer, `astro-ph/0204199`, submitted to *App. J. Lett.*

[44] M. Rampp, R. Buras, H.T. Janka, G. Raffelt, `astro-ph/0203493`.

[45] A. Burrows, T.A. Thompson, `astro-ph/0210212`.

[46] A. Mezzacappa, M. Liebendorfer, O.E. Messer, W.R. Hix, F.K. Thielemann, S.W. Bruenn, *Phys. Rev. Lett.* **86**, 1935 (2001).

[47] W. Keil, H.T. Janka, *Astron. Astrophys.* **296**, 145 (1995).

[48] J.A. Pons, S. Reddy, M. Prakash, J.M. Lattimer, J.A. Miralles, *Astrophys. J.* **513**, 780 (1999).

[49] J.A. Pons, A.W. Steiner, M. Prakash, J.M. Lattimer, *Phys. Rev. Lett.* **86**, 5223 (2001).

[50] M. Prakash, J.M. Lattimer, J.A. Pons, A.W. Steiner, S. Reddy, *Lect. Notes Phys.* **578**, 364 (2001).

[51] R.F. Sawyer, *Phys. Rev.* **D11**, 2740 (1975).

[52] B. Friman, O.V. Maxwell, *Astrophys. J.* **232**, 541 (1979).

[53] N. Iwamoto, C.J. Pethick, *Phys. Rev.* **D25**, 313 (1982).

[54] R.F. Sawyer, *Phys. Rev.* **C40**, 865 (1989).

[55] C.J. Horowitz, K. Wehrberger, *Nucl. Phys.* **A531**, 665 (1991); *Phys. Rev. Lett.* **66**, 272 (1991); *Phys. Lett.* **B226**, 236 (1992).

[56] G. Raffelt, D. Seckel, *Phys. Rev.* **D52**, 1780 (1995).

[57] G. Sigl, *Phys. Rev. Lett.* **76**, 2625 (1996).

[58] S. Reddy, J. Pons, M. Prakash, J.M. Lattimer, In *Stellar Evolution, Stellar Explosions and Galactic Chemical Evolution*, ed. T. Mezzacappa, IOP Publishing, Bristol 1997, p. 585.

[59] S. Reddy, M. Prakash, *Astrophys. J.* **423**, 689 (1997).

[60] M. Prakash, S. Reddy: In *Nuclear Astrophysics*, ed. M. Buballa, W. Nörenberg, J. Wambach, A. Wirzba, GSI: Darmstadt 1997, p. 187.

[61] S. Reddy, M. Prakash, J.M. Lattimer, *Phys. Rev.* **D58**, 013009 (1998).

[62] S. Reddy, M. Prakash, J.M. Lattimer, J.A. Pons, *Phys. Rev.* **C59**, 2888 (1999).

[63] A. Burrows, R.F. Sawyer, *Phys. Rev.* **C58**, 554 (1998).

[64] A. Burrows, R.F. Sawyer, *Phys. Rev.* **C59**, 510 (1999).

[65] C. Hanhart, D.R. Phillips, S. Reddy, *Phys. Lett.* **B499**, 9 (2001).

[66] S. Reddy, G.F. Bertsch, M. Prakash, *Phys. Lett.* **B475**, 1 (2000).

[67] M. Christiansen, N.K. Glendenning, J. Schaffner-Bielich, *Phys. Rev.* **C62**, 025804 (2000).

[68] G.W. Carter, S. Reddy, *Phys. Rev.* **D62**, 103002 (2000).

[69] R.D. Pisarski, D.H. Rischke, *Phys. Rev.* **D60**, 094013 (1999).

[70] P. Jaikumar, M. Prakash, T. Schafer, *Phys. Rev.* **D66**, 063003 (2002).

[71] S. Reddy, M. Sadzikowski, M. Tachibana, `nucl-th/0203011`.